Meyer, H.; Angioni, C.; Albert, C. G.; Arden, Nils; Arredondo Parra, R.; Asunta, O.; De Baar, M.; Balden, M.; Bandaru, V.; Behler, K.; Bergmann, A.; Bernardo, J.; Bernert, M.; Biancalani, A.; Bilato, R.; Birkenmeier, G.; Blanken, T. C.; Bobkov, V.; Bock, A.; Bolzonella, T.; Bortolon, A.; Böswirth, B.; Bottereau, C.; Bottino, A.; Van Den Brand, H.; Brezinsek, S.; Brida, D.; Brochard, F.; Bruhn, C.; Buchanan, J.; Buhler, A.; Burckhart, A.; Camenen, Y.; Carlton, D.; Carr, M.; Carralero, D.; Castaldo, C.; Cavedon, M.; Cazzaniga, C.; Ceccuzzi, S.; Challis, C.; Chankin, A.; Chapman, S.; Cianfarani, C.; Clairet, F.; Coda, S.; Coelho, R.; Coenen, J. W.; Colas, L.; Conway, G. D.

Overview of physics studies on ASDEX Upgrade

Please cite the original version:
Meyer, H., Angioni, C., Albert, C. G., Arden, N., Arredondo Parra, R., Asunta, O., De Baar, M., Balden, M., Bandaru, V., Behler, K., Bergmann, A., Bernardo, J., Bernert, M., Biancalani, A., Bilato, R., Birkenmeier, G., Blanken, T. C., Bobkov, V., Bock, A., ... Zohm, H. (2019). Overview of physics studies on ASDEX Upgrade. *Nuclear Fusion*, *59*(11), Article 112014. https://doi.org/10.1088/1741-4326/ab18b8

PAPER • OPEN ACCESS

Overview of physics studies on ASDEX Upgrade

To cite this article: H. Meyer *et al* 2019 *Nucl. Fusion* **59** 112014

View the article online for updates and enhancements.

Recent citations

- Heat transport driven by the ion temperature gradient and electron temperature gradient instabilities in ASDEX Upgrade H-modes
  F. Ryter *et al*

- Physics research on the TCV tokamak facility: from conventional to alternative scenarios and beyond
  S. Coda *et al*

Overview of physics studies on ASDEX Upgrade

H. Meyer[2] for the AUG Team: D. Aguiam[3], C. Angioni[1], C.G. Albert[1,41], N. Arden[1], R. Arredondo Parra[1], O. Asunta[4], M. de Baar[5], M. Balden[1], V. Bandaru[1], K. Behler[1], A. Bergmann[1], J. Bernardo[3], M. Bernert[1], A. Biancalani[1], R. Bilato[1], G. Birkenmeier[1,6],T.C. Blanken[48], V. Bobkov[1], A. Bock[1],T. Bolzonella[7], A. Bortolon[31], B. Böswirth[1], C. Bottereau[8], A. Bottino[1], H. van den Brand[5], S. Brezinsek[9], D. Brida[1,6], F. Brochard[10], C. Bruhn[1,6], J. Buchanan[2], A. Buhler[1], A. Burckhart[1],Y. Camenen[49], D. Carlton[1], M. Carr[2], D. Carralero[1,44], C. Castaldo[53], M. Cavedon[1], C. Cazzaniga[7], S. Ceccuzzi[53], C. Challis[2], A. Chankin[1], S. Chapman[47], C. Cianfarani[53], F. Clairet[8], S. Coda[12], R. Coelho[3], J.W. Coenen[9], L. Colas[8], G.D. Conway[1], S. Costea[13], D.P. Coster[1],T.B. Cote[39], A. Creely[38], G. Croci[11], G. Cseh[14], A. Czarnecka[15], I. Cziegler[29], O. D'Arcangelo[53], P. David[1], C. Day[16], R. Delogu[11], P. de Marné[1], S.S. Denk[1,6], P. Denner[9], M. Dibon[1], A. Di Siena[1], D. Douai[8], A. Drenik[1], R. Drube[1], M. Dunne[1], B.P. Duval[12], R. Dux[1],T. Eich[1], S. Elgeti[1], K. Engelhardt[1], B. Erdös[14], I. Erofeev[1], B. Esposito[53], E. Fable[1], M. Faitsch[1], U. Fantz[1], H. Faugel[1], I. Faust[1], F. Felici[12], J. Ferreira[3], S. Fietz[1], A. Figuereido[3], R. Fischer[1], O. Ford[54], L. Frassinetti[17], S. Freethy[1,2,38], M. Fröschle[1], G. Fuchert[54], J.C. Fuchs[1], H. Fünfgelder[1], K. Galazka[15], J. Galdon-Quiroga[1,19], A. Gallo[8], Y. Gao[9], S. Garavaglia[11], A. Garcia-Carrasco[17], M. Garcia-Muñoz[19], B. Geiger[54], L. Giannone[1], L. Gil[3], E. Giovannozzi[53], C. Gleason-González[16], S. Glöggler[1,6], M. Gobbin[7], T. Görler[1], I. Gomez Ortiz[1], J. Gonzalez Martin[19], T. Goodman[12], G. Gorini[52], D. Gradic[54], A. Gräter[1], G. Granucci[11], H. Greuner[1], M. Griener[1,6], M. Groth[4], A. Gude[1], S. Günter[1], L. Guimarais[3], G. Haas[1], A.H. Hakola[20], C. Ham[2],T. Happel[1], N. den Harder[1], G.F. Harrer[21], J. Harrison[2], V. Hauer[16],T. Hayward-Schneider[1], C.C. Hegna[39], B. Heinemann[1], S. Heinzel[22],T. Hellsten[18], S. Henderson[2], P. Hennequin[23], A. Herrmann[1], M.F. Heyn[41], E. Heyn[24], F. Hitzler[1,6], J. Hobirk[1], K. Höfler[1], M. Hölzl[1],T. Höschen[1], J.H. Holm[25], C. Hopf[1], W.A. Hornsby[1], L. Horvath[26], A. Houben[10], A. Huber[9], V. Igochine[1],T. Ilkei[14], I. Ivanova-Stanik[15], W. Jacob[1], A.S. Jacobsen[1], F. Janky[1], A. Jansen van Vuuren[54], A. Jardin[43], F. Jaulmes[5,40], F. Jenko[1],T. Jensen[25], E. Joffrin[8], C.-P. Käsemann[1], A. Kallenbach[1], S. Kálvin[14], M. Kantor[5], A. Kappatou[1], O. Kardaun[1], J. Karhunen[5], S. Kasilov[41,42], Y. Kazakov[28], W. Kernbichler[41], A. Kirk[2], S. Kjer Hansen[1,25], V. Klevarova[27], G. Kocsis[14], A. Köhn[1], M. Koubiti[49], K. Krieger[1], A. Krivska[28], A. Krämer-Flecken[9], O. Kudlacek[1],T. Kurki-Suonio[4], B. Kurzan[1], B. Labit[12], K. Lackner[1], F. Laggner[21,31], P.T. Lang[1], P. Lauber[1], A. Lebschy[1,6], N. Leuthold[1], M. Li[1], O. Linder[1], B. Lipschultz[29], F. Liu[51], Y. Liu[2,18], A. Lohs[1], Z. Lu[1],T. Luda di Cortemiglia[1], N.C. Luhmann[30], R. Lunsford[31],T. Lunt[1], A. Lyssoivan[28],T. Maceina[1], J. Madsen[25],

R. Maggiora[50], H. Maier[1], O. Maj[1], J. Mailloux[2], R. Maingi[31], E. Maljaars[48],
P. Manas[1], A. Mancini[11], A. Manhard[1], M.-E. Manso[3], P. Mantica[11],
M. Mantsinen[32,46], P. Manz[1], M. Maraschek[1], C. Martens[1], P. Martin[7],
L. Marrelli[7], A. Martitsch[41], M. Mayer[1], D. Mazon[8], P.J. McCarthy[33],
R. McDermott[1], H. Meister[1], A. Medvedeva[1,10], R. Merkel[1], A. Merle[12],
V. Mertens[1], D. Meshcheriakov[1], O. Meyer[8], J. Miettunen[5], D. Milanesio[50],
F. Mink[1,6], A. Mlynek[1], F. Monaco[1], C. Moon[1], F. Nabais[3], A. Nemes-Czopf[15],
G. Neu[1], R. Neu[1,34], A.H. Nielsen[25], S.K. Nielsen[25], V. Nikolaeva[1,3,6],
M. Nocente[52], J.-M. Noterdaeme[1,27], I. Novikau[1], S. Nowak[12], M. Oberkofler[1],
M. Oberparleiter[35], R. Ochoukov[1], T. Odstrcil[1,10], J. Olsen[25], F. Orain[1,23],
F. Palermo[1], O. Pan[1,6], G. Papp[1], I. Paradela Perez[4], A. Pau[36], G. Pautasso[1],
F. Penzel[1], P. Petersson[20], J. Pinzón Acosta[1,6], P. Piovesan[7], C. Piron[7],
R. Pitts[51], U. Plank[1], B. Plaum[24], B. Ploeckl[1], V. Plyusnin[3], G. Pokol[28],
E. Poli[1], L. Porte[12], S. Potzel[1], D. Prisiazhniuk[1,6], T. Pütterich[1],
M. Ramisch[24], J. Rasmussen[25], G.A. Rattá[44], S. Ratynskaia[17], G. Raupp[1],
G.L. Ravera[53], D. Réfy[14], M. Reich[1], F. Reimold[9,54], D. Reiser[9], T. Ribeiro[1],
J. Riesch[1], R. Riedl[1], D. Rittich[1], J.F. Rivero-Rodriguez[19], G. Rocchi[53],
M. Rodriguez-Ramos[19], V. Rohde[1], A. Ross[1], M. Rott[1], M. Rubel[17], D. Ryan[2],
F. Ryter[1], S. Saarelma[2], M. Salewski[25], A. Salmi[4], L. Sanchis-Sanchez[19],
J. Santos[3], O. Sauter[12], A. Scarabosio[1], G. Schall[1], K. Schmid[1],
O. Schmitz[32], P.A. Schneider[1], R. Schrittwieser[13], M. Schubert[1],
T. Schwarz-Selinger[1], J. Schweinzer[1], B. Scott[1], T. Sehmer[1], E. Seliunin[3],
M. Sertoli[1], A. Shabbir[27], A. Shalpegin[12], L. Shao[37], S. Sharapov[2], G. Sias[36],
M. Siccinio[1,45], B. Sieglin[1], A. Sigalov[1], A. Silva[3], C. Silva[3], D. Silvagni[1],
P. Simon[1,10,24], J. Simpson[2], E. Smigelskis[1], A. Snicker[4], C. Sommariva[8],
C. Sozzi[11], M. Spolaore[7], A. Stegmeir[1], M. Stejner[25], J. Stober[1], U. Stroth[1,6],
E. Strumberger[1], G. Suarez[1], H.-J. Sun[1], W. Suttrop[1], E. Sytova[1],
T. Szepesi[14], B. Tál[1,14], T. Tala[20], G. Tardini[1], M. Tardocchi[11], M. Teschke[1],
D. Terranova[7], W. Tierens[1], E. Thorén[17], D. Told[1], P. Tolias[17], O. Tudisco[53],
W. Treutterer[1], E. Trier[1], M. Tripský[28], M. Valisa[7], M. Valovic[2], B. Vanovac[1,5],
D. van Vugt[48,51], S. Varoutis[16], G. Verdoolaege[28,27], N. Vianello[7], J. Vicente[3],
T. Vierle[1], E. Viezzer[19], U. von Toussaint[1], D. Wagner[1], N. Wang[8], X. Wang[1],
M. Weiland[1], A.E. White[38], S. Wiesen[9], M. Willensdorfer[1], B. Wiringer[1],
M. Wischmeier[1], R. Wolf[54], E. Wolfrum[1], L. Xiang[37], Q. Yang[37], Z. Yang[1],
Q. Yu[1], R. Zagórski[15], I. Zammuto[1], W. Zhang[1,27], M. van Zeeland[18],
T. Zehetbauer[1], M. Zilker[1], S. Zoletnik[14], H. Zohm[1] and the EUROfusion
MST1 Team[a]

[1] Max-Planck-Institut für Plasmaphysik, D-85748 Garching, Germany
[2] United Kingdom Atomic Energy Authority (CCFE), Culham Science Centre, Abingdon, Oxon, OX14 3DB, United Kingdom of Great Britain and Northern Ireland
[3] Instituto de Plasmas e Fusão Nuclear, Instituto Superior Técnico, Universidade de Lisboa, Av. Rovisco Pais 1, 1049-001 Lisboa, Portugal
[4] Department of Applied Physics, Aalto University, PO Box 14100, FI-00076 Aalto, Finland
[5] DIFFER—Dutch Institute for Fundamental Energy Research, De Zaale 20, 5612 AJ Eindhoven, Netherlands
[6] Physik-Department E28, Technische Universität München, D-85748 Garching, Germany
[7] Consorzio RFX, Corso Stati Uniti 4, 35127 Padova, Italy
[8] CEA, IRFM, F-13108 Saint Paul Lez Durance, France
[9] Forschungszentrum Jülich GmbH, Institut für Energie- und Klimaforschung—Plasmaphysik, 52425 Jülich, Germany
[10] Institut Jean Lamour, Université de Lorraine, Vandoeuvre-lés-Nancy, 54000 Nancy, France
[11] IFP-CNR, via R. Cozzi 53, 20125 Milano, Italy
[12] Ecole Polytechnique Fédérale de Lausanne (EPFL), Swiss Plasma Center (SPC), CH-1015 Lausanne, Switzerland

[a] See the author list of Labit *et al* [136].

[13] Institute for Ion Physics and Applied Physics, Universität Innsbruck, Technikerstraße 25, 6020 Innsbruck, Austria

[14] Wigner Research Centre for Physics, POB 49, H-1525 Budapest, Hungary

[15] Institute of Plasma Physics and Laser Microfusion, Hery 23, 01-497 Warsaw, Poland

[16] Karlsruhe Institute of Technology, PO Box 3640, D-76021 Karlsruhe, Germany

[17] Fusion Plasma Physics, EES, KTH, SE-10044 Stockholm, Sweden

[18] General Atomics, 3550 General Atomics Court, San Diego, CA 92121-1122, United States of America

[19] Department of Atomic, Molecular and Nuclear Physics, University of Seville, 41012 Seville, Spain

[20] VTT Technical Research Centre of Finland, PO Box 1000, FI-02044 VTT, Finland

[21] Institute of Applied Physics, Technische Universität Wien, Wiedner Hauptstraße 8-10, 1040 Wien, Austria

[22] Max-Planck Computing and Data Facility, Boltzmannstr. 2, D-85748 Garching, Germany

[23] Laboratoire de Physique des Plasmas, CNRS UMR7648, Ecole Polytechnique, 91128 Palaiseau, France

[24] Institut für Grenzflächenverfahrenstechnik und Plasmatechnologie, Pfaffenwaldring 31, D-70569 Stuttgart, Germany

[25] Department of Physics, Technical University of Denmark, Bldg 309, DK-2800 Kgs Lyngby, Denmark

[26] Institute of Nuclear Techniques, Budapest University of Technology and Economics, PO Box 91, H-1521 Budapest, Hungary

[27] Department of Applied Physics UG (Ghent University) St-Pietersnieuwstraat 41 B-9000 Ghent, Belgium

[28] Laboratory for Plasma Physics Koninklijke Militaire School—Ecole Royale Militaire Renaissancelaan 30 Avenue de la Renaissance B-1000, Brussels, Belgium

[29] Department of Physics, York Plasma Institute, University of York, Heslington, York, YO10 5DD, United Kingdom of Great Britain and Northern Ireland

[30] University of California at Davis, Davis, CA 95616, United States of America

[31] Princeton Plasma Physics Laboratory, 100 Stellarator Road, Princeton, PO Box 451, NJ 08540, United States of America

[32] Barcelona Supercomputing Center, Jordi Girona 29, 08034 Barcelona, Spain

[33] Physics Department, University College Cork (UCC), Cork, Ireland

[34] Fakultät Maschinenwesen, Technische Universität München, D-85748 Garching, Germany

[35] Department of Earth and Space Sciences, Chalmers University of Technology, SE-41296 Gothenburg, Sweden

[36] Department of Electrical and Electronic Engineering, University of Cagliari, Piazza d'Armi 09123 Cagliari, Italy

[37] Institute of Plasma Physics, Chinese Academy of Sciences, Hefei 230031, People's Republic of China

[38] Plasma Science and Fusion Center, MIT, Cambridge, MA, United States of America

[39] Department of Engineering Physics, University of Wisconsin-Madison, Madison, WI 53706, United States of America

[40] Institute of Plasma Physics AS CR, Za Slovankou 1782/3, 182 00 Praha 8, Czech Republic

[41] Fusion@ÖAW, Institut für Theoretische Physik—Computational Physics, TU Graz, Petersgasse 16, A-8010 Graz, Austria

[42] Institute of Plasma Physics, National Science Center Kharkov Institute of Physics and Technology, Ul. Akademicheskaya 1, 61108 Kharkov, Ukraine

[43] Institute of Nuclear Physics Polish Academy of Sciences (IFJ PAN), PL-31-342, Krakow, Poland

[44] Laboratorio Nacional de Fusión, CIEMAT, Av. Complutense 40, 28040 Madrid, Spain

[45] EUROfusion PPP&T, Boltzmannstraße 2, 85748, Garching, Germany

[46] ICREA, Pg. Lluís Companys 23, 08010 Barcelona, Spain

[47] Department of Physics, Centre for Fusion, Space and Astrophysics, Warwick University, Coventry CV4 7AL, United Kingdom of Great Britain and Northern Ireland

[48] Eindhoven University of Technology PO Box 513, 5600 MB Eindhoven, Netherlands

[49] CNRS, Aix-Marseille Université, PIIM UMR7345, Marseille, France

[50] Dipartimento di Elettronica e Telecomunicazioni (DET), Politecnico di Torino, Torino, Italy

[51] ITER Organization, Route de Vinon, CS 90 046, 13067 Saint Paul Lez Durance, France

[52] Dipartimento di Fisica, Università di Milano-Bicocca, Piazza della Scienza 3, 20126 Milano, Italy

[53] ENEA, Fusion and Nuclear Safety Departement, C.R. Frascati, Via E. Fermi 45, 00044 Frascati (Roma), Italy

[54] Max-Planck-Institut für Plasmaphysik, Teilinstitut Greifswald, D-17491 Greifswald, Germany

E-mail: hendrik.meyer@ukaea.uk

CrossMark

Abstract

The ASDEX Upgrade (AUG) programme, jointly run with the EUROfusion MST1 task force, continues to significantly enhance the physics base of ITER and DEMO. Here, the full tungsten wall is a key asset for extrapolating to future devices. The high overall heating power, flexible heating mix and comprehensive diagnostic set allows studies ranging from mimicking the scrape-off-layer and divertor conditions of ITER and DEMO at high density to fully non-inductive operation ($q_{95} = 5.5$, $\beta_N \leqslant 2.8$) at low density. Higher installed electron cyclotron resonance heating power $\leqslant 6$ MW, new diagnostics and improved analysis techniques have further enhanced the capabilities of AUG.

Stable high-density H-modes with $P_{\text{sep}}/R \leqslant 11$ MW m^{-1} with fully detached strike-points have been demonstrated. The ballooning instability close to the separatrix has been identified as a potential cause leading to the H-mode density limit and is also found to play an important role for the access to small edge-localized modes (ELMs). Density limit disruptions have been successfully avoided using a path-oriented approach to disruption handling and progress has been made in understanding the dissipation and avoidance of runaway electron beams. ELM suppression with resonant magnetic perturbations is now routinely achieved reaching transiently $H_{\text{H98(y,2)}} \leqslant 1.1$. This gives new insight into the field penetration physics, in particular with respect to plasma flows. Modelling agrees well with plasma response measurements and a helically localised ballooning structure observed prior to the ELM is evidence for the changed edge stability due to the magnetic perturbations. The impact of 3D perturbations on heat load patterns and fast-ion losses have been further elaborated.

Progress has also been made in understanding the ELM cycle itself. Here, new fast measurements of T_i and E_r allow for inter ELM transport analysis confirming that E_r is dominated by the diamagnetic term even for fast timescales. New analysis techniques allow detailed comparison of the ELM crash and are in good agreement with nonlinear MHD modelling. The observation of accelerated ions during the ELM crash can be seen as evidence for the reconnection during the ELM. As type-I ELMs (even mitigated) are likely not a viable operational regime in DEMO studies of 'natural' no ELM regimes have been extended. Stable I-modes up to $n/n_{\text{GW}} \leqslant 0.7$ have been characterised using β-feedback.

Core physics has been advanced by more detailed characterisation of the turbulence with new measurements such as the eddy tilt angle—measured for the first time—or the cross-phase angle of T_e and n_e fluctuations. These new data put strong constraints on gyro-kinetic turbulence modelling. In addition, carefully executed studies in different main species (H, D and He) and with different heating mixes highlight the importance of the collisional energy exchange for interpreting energy confinement. A new regime with a hollow T_e profile now gives access to regimes mimicking aspects of burning plasma conditions and lead to nonlinear interactions of energetic particle modes despite the sub-Alfvénic beam energy. This will help to validate the fast-ion codes for predicting ITER and DEMO.

Keywords: nuclear fusion, magnetic confinement, tokamak physics, ITER, DEMO

(Some figures may appear in colour only in the online journal)

1. Introduction and technical improvements

The ASDEX Upgrade (AUG) tokamak is the only medium sized ($R_{\text{geo}} = 1.65$ m, $a = 0.5$ m, $B_t \leqslant 3.2$ T, $I_p \leqslant 1.4$ MA, $\delta \leqslant 0.5, \kappa \leqslant 1.8$) D shaped tokamak with a full metal—mainly tungsten (W)—wall [1]. W is currently regarded as the most viable material for plasma facing components (PFC) in a future fusion reactor. The programme on AUG is geared towards developing the physics basis for ITER and (EU)-DEMO and is jointly executed with the EUROfusion Medium Size Tokamak task force (EU-MST1). Integrated scenario development to prepare future device operation, detailed physics studies to improve predictability of fusion devices and testing of fusion relevant technologies are all part of the comprehensive programme. Here, the full tungsten wall not only requires efficient techniques to control W accumulation, but also modifies the edge and scrape-off-layer (SOL) conditions (e.g. due to changes of the neutral influx from the wall). The high overall installed flexible heating power of $P_{\text{NBI}} \leqslant 20$ MW neutral beam injection (NBI), $P_{\text{ICRF}} \leqslant 7$ MW ion cyclotron range of frequency heating (ICRF) and $P_{\text{ECRH}} \leqslant 6$ MW dual frequency 140 GHz (4.8 MW with 105 GHz) electron cyclotron resonance heating (ECRH, coupled $\leqslant 5.4$ MW with 140 GHz) allows the simulation of reactor relevant divertor and
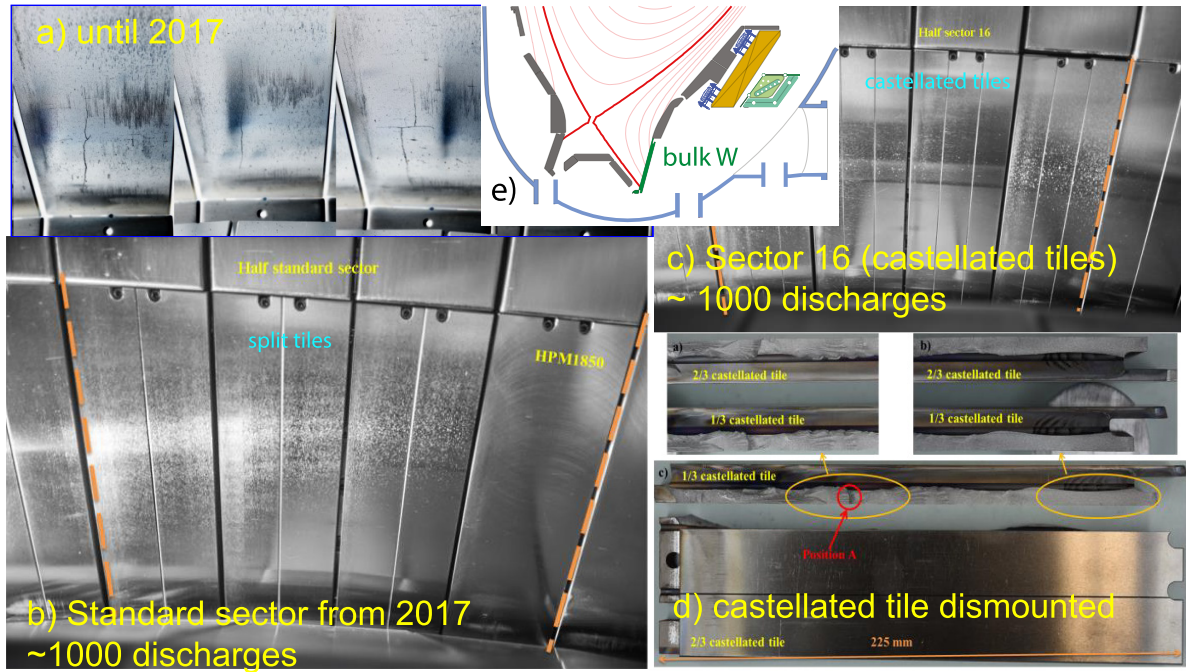
Figure 1. Divertor tiles on AUG made from (*a*) W before 2017, (*b*) 1/2 standard sector (split W and HPM1850), (*c*) sector 16 with double castellated design and (*d*) dismounted castellated tiles showing deep cracks. The inlet (*e*) shows a poloidal cross section of the divertor with the bulk tungsten (W) tiles in the outer divertor shown in the photos marked in green.

SOL conditions in H-mode (see section 2) as well as access to fully non-inductive scenarios [2] (see section 4). All heating systems are specified for 10 s pulse length.

Aside from various diagnostic upgrades the most noteworthy improvements of the device capabilities are the new ECRH III system [3] and the new/improved power supplies for the 16 in-vessel 3D perturbation coils (B-coils) [4]. ECRH III operated at half capacity (two gyrotrons) from 2017 and will reach its full capacity with four gyrotrons shortly allowing for up to 7 MW coupled power at 140 GHz. So far $P_{ECRH} = 5.5$ MW have been coupled during the commissioning of the last two gyrotrons. The 16 B-coils now each have their own faster power supply allowing a great flexibility for the application of magnetic perturbations (MP) (see section 3).

To prevent previously observed deep vertical cracking of the W tiles in the divertor (see figure 1(*a*)) [5] a new design was employed in 2017 (figures 1(*b*) and (*c*)) [6]. The standard divertor sector consists of eight tiles. The two outermost positions, which see the highest electromagnetic forces (loads), were equipped with more ductile heavy W alloy tiles (HPM1850, containing Fe and Ni) [7] and in the six remaining positions split tiles were mounted to reduce the thermomechanical stresses (figure 1(*b*)). In addition three sectors had special setups: (1) with castellated W tiles (figure 1(*c*)); (2) with target clamping and wide W tiles; (3) with optimized target clamping and split W tiles. Inspection after about 1000 discharges with > 40 discharges with $P_{heat} > 15$ MW (maximum $P_{heat} = 20$ MW) showed that in setup (3) as well as in the standard setup the vertical cracks were completely suppressed with no macroscopic damage for correctly aligned tiles (see figure 1(*b*)). For setups (1) and (2), however, deep

cracks in the W tiles were observed (figure 1(*d*)) [8]. For the next campaign the standard split tile setup is mounted in all sectors, but with titanium clamps. The performance of the HPM1850 tiles was also notable and the melt behaviour (see section 2) for misaligned HPM1850 tiles is similar to that of pure W. No Fe or Ni has been observed in the plasma [9].

2. Divertor and edge

The interplay between PFC, divertor and SOL and the plasma edge is still a critical issue in particular for W PFCs [10]. On the one hand the transients due to edge localised modes (ELMs) pose a large threat to future devices as a recent multi-machine scaling for the energy fluence at the target $\varepsilon_{||} \propto p_{ped}R_{geo}$ (p_{ped}: pedestal top pressure, R_{geo}: geometric major radius) still extrapolates to at least three times higher heat loads than viable for the integrity of currently foreseen materials in ITER [11–13]. On the other hand the necessity of high divertor neutral pressure requiring high fuelling rates leads to a degradation of plasma confinement due to an outward shift of the pressure profile at the edge [14–16]. This shift can also be parametrised by the separatrix density $n_{e,sep}$ and on AUG a clear correlation of reduced edge stability and therefore reduced confinement with $n_{e,sep}$ is observed. This is attributed to the presence of the high field side high density (HFSHD) region the dynamics of which has been further characterised by high and low-field side reflectometer measurements [17] and modelled with a 2D fluid code (SOLPS5.0) [18]. The modelled and observed dynamics of the HFSHD region also reconcile the confinement improvement observed with impurity seeding (N$_2$, CD$_4$ and Ne).

ITER and DEMO will operate at high $n_{e,sep}$. Analysis of Thomson scattering data from AUG and JET suggests that there could be a maximum achievable $n_{e,sep}$ limited by the ballooning stability just inside the separatrix [19], which is responsible for the H-mode density limit (HDL). As can be seen from figure 2 the ballooning parameter increases linearly with the separatrix density normalised to the Greenwald density n_{GW} until it reaches $n_{e,sep}/n_{GW} \approx 0.3$ or $\alpha_{sep} = 2\mu_0 R q_{cyl}^2 p_{sep}/(B_t^2 \langle \lambda_p \rangle) \approx 1.5$, when confinement starts to degrade. Here $q_{cyl} = 2\pi ab B_t/(\mu_0 I_p R)$ is the cylindrical q (a, b are the half width and half height of the plasma), p_{sep} is the pressure at the separatrix and λ_p is the pressure fall off length in the mid-plane SOL. The linear dependence of $\alpha_{sep} \propto n_{e,sep}/n_{GW}$ reflects the multi-machine scaling of $\lambda_q \approx 1/2\lambda_p$ but the data seem not to exceed a critical ballooning parameter $\alpha_{sep}^{crit} \approx 2 \cdots 2.5$. It is conjectured that above this critical value turbulence increases leading to enhanced density transport and ultimately the loss of H-mode. Using the multi-machine scaling for the SOL decay length λ_q and assuming $\lambda_p \approx 2\lambda_q$—as is found by direct comparison of both latter quantities—a critical normalised density of $n_{e,sep}^{crit}/n_{GW} \approx 6 \cdot \alpha_{sep}^{crit} \cdot A^{-7/2} \left[(1+\kappa^2)/2\right]^{-6/7} \cdot P_{sep}^{-1/7} \approx 0.5$ (P_{sep}: power flowing over the separatrix) for the HDL can be calculated, though strictly the scaling does not apply to high density.

The increased turbulence leads to a flattening of ∇n_e at the separatrix and a narrowing of the pedestal. Here, the electron temperature at the separatrix $T_{e,sep} \approx 100$ eV drops slightly by about 10–20 eV when approaching the HDL. The increase of the normalised density from about 0.35 to 0.5 is mainly compensated by a relaxation of the pressure gradient so that the ballooning parameter is staying constant. With high shaping and reduced magnetic edge shear $s = \langle \mathrm{d}q/\mathrm{d}r \rangle / \langle q \rangle$ this can lead to a stabilisation of peeling–ballooning modes and a stable high confinement small-ELM regime [13, 20]. On AUG also a strong correlation between the divertor pressure $p_{0,div}$ and $n_{e,sep} \propto p_{0,div}^{0.31}$ has been found [21] (coefficient of determination $R^2 = 0.7$, RMS = 17%). This correlation observed for discharges with and without N_2 seeding depends only weakly on other experimental parameters. Therefore, under stationary conditions the engineering parameter $p_{0,div}$ is directly linked to plasma confinement, though some dependence on the opacity of the SOL and the dynamic of the HFSHD region remain. Both in H-mode ($P_{heat} = 6.5$ MW) and L-mode, as the effective collisionality in the divertor increases, the SOL n_e profile tends to flatten forming a density shoulder commonly attributed to a large blob-size of the filamentary cross-field transport in the SOL. However, in H-mode a flattening is only observed with increased blob-size if also $p_{0,div}$ increases [22]. The physics of the shoulder formation is important as for example in L-mode 20% of the power flux can be observed in the far SOL [23]. Here, the ions are carrying a large fraction of the power flux into the SOL and $T_i \approx 3T_e$ is measured in the mid-plane [23] as previously on MAST [24]. These power fluxes are not carried into the divertor and could pose a problem to the first wall in ITER and DEMO [23].
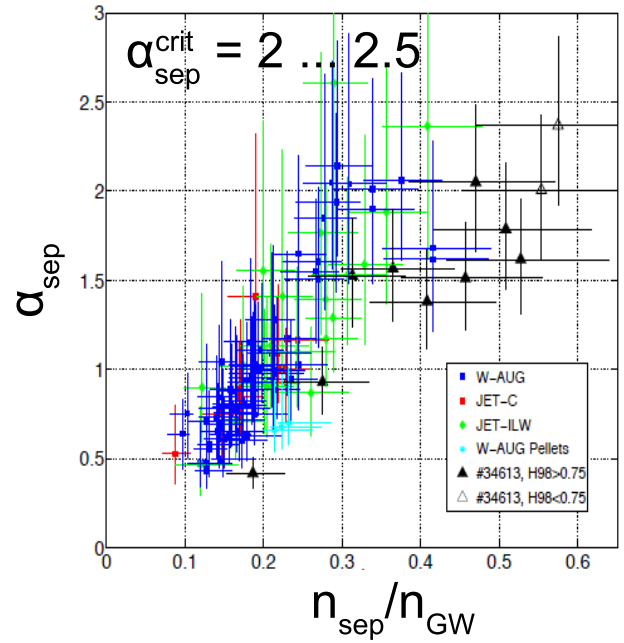
Figure 2. Relation of the ballooning parameter at the separatrix α_{sep} to the normalised separatrix density for AUG and JET discharges. Reproduced courtesy of IAEA. Figure from [19]. © EURATOM 2018.

High $p_{0,div}$ and N_2 seeding is used to promote detachment. On AUG stable operation with fully detached strike points has been achieved with up-to $P_{sep}/R \lesssim 11$ MW m^{-1} using N_2 and Ar seeding. With the use of N also ammonia (ND_3) is formed, which for fusion power plants increases the in-vessel T inventory. The ND_3 production has now been characterised in AUG and residual gas analysis measurements have been confirmed by divertor spectroscopy. ND_3 is formed in particular on the peripheral surface areas in the inner divertor [25, 26].

Not only $n_{e,sep}$ is important for the confinement but also correlations with the SOL T_e decay length, $\lambda_{T_e,u}$ have been found. The study of the SOL upstream T_e profile on AUG [27, 28] shows that, for detached plasmas, the SOL upstream electron temperature profile is observed to be broader than for an equivalent attached plasma under certain conditions. By comparing $\lambda_{T_e,u}$ with the global energy confinement, it is found that the discharges with broadened profiles also have degraded confinement, while those with unchanged profiles have similar confinement to that in attached plasmas. In case of N_2 seeding, for a fixed plasma current, the pedestal top pressure can be increased significantly with high heating power, while almost no influence on the SOL T_e decay length, $\lambda_{T_e,u}$, is observed.

To optimise edge performance with tolerable exhaust and confinement properties an improved understanding of the ELM cycle is needed. Fast measurements of E_r during type-I ELMs as well as during limit cycle oscillations show that the field is dominated by the diamagnetic term $E_r \approx \nabla p_i/n$ even on the fast time scale following the recovery of n_e [29]. In figure 3 the type-I ELM synchronised evolution of several quantities in the pedestal region are shown: $\min(E_r)$ from (a) neoclassical (NC) calculations using NEOART and (b) the impurity force balance; the steepest gradients of (c) T_i, (d) T_e
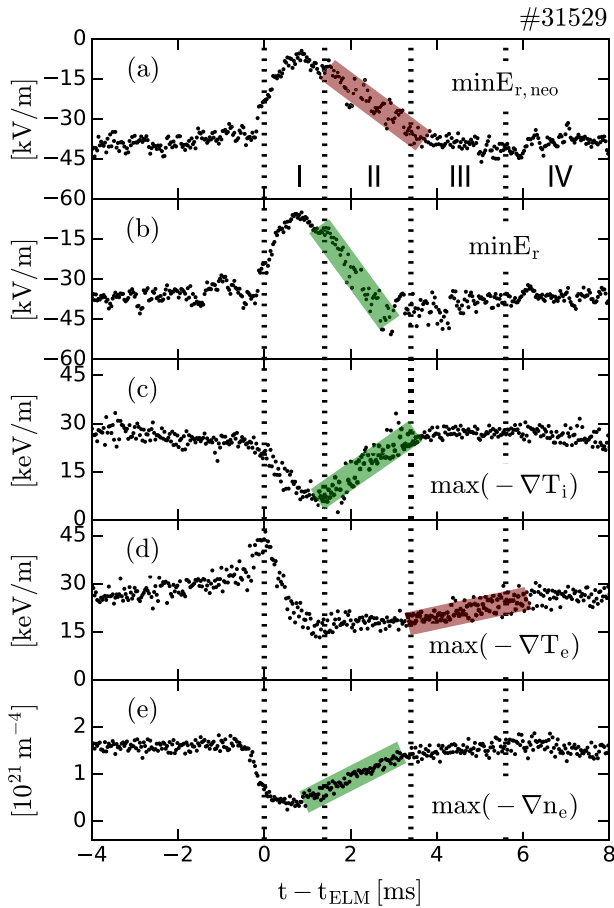
Figure 3. ELM synchronised evolution of the minimum E_r from (*a*) neoclassical predictions and (*b*) CXRS measurements as well as the steepest gradients of (*c*) T_i, (*d*) T_e and (*e*) n_e during a type-I ELM cycle.

and (e) n_e ($\rho_{pol} \sim 0.99$). These have been measured using fast charge exchange recombination spectroscopy (CXRS) on He (E_r, T_i), electron cyclotron emission (ECE) (T_e) and lithium beam spectroscopy (n_e). Comparing figures 3(*a*) and (*b*) it can be seen that only during the short ∇T_i and ∇n_e recovery phase just after the ELM crash does E_r deviate from the NC prediction. Interestingly the ion and electron temperatures recover on different time scales. The three different phases (II–IV: see figure 3(*a*)) can be related to magnetohydrodynamic (MHD) activity at different frequencies, with phase I being the ELM crash itself. In particular a high frequency $n \sim 11$ mode (typical $f > 200$ kHz) in the steep pedestal gradient region close to the E_r minimum has been identified during the pedestal recovery coinciding with the clamping of the ∇T_e and hence ∇p [30]. This mode showing no ballooning structure is present in D, H and He discharges. In the period the high frequency mode is present also a low frequency mode ($f \approx 4$–8 kHz) located in the upper half of the pedestal is observed and has been characterised using ECE imaging [31]. The mode sometimes has a slowing down characteristic during the ELM cycle, which may be attributed to the widening of the pedestal. Bi-coherence analysis suggests a nonlinear coupling between high and low frequency modes due to their similar mode structure and spatial proximity. However, the frequency of the high frequency mode shows no slowing down supporting the
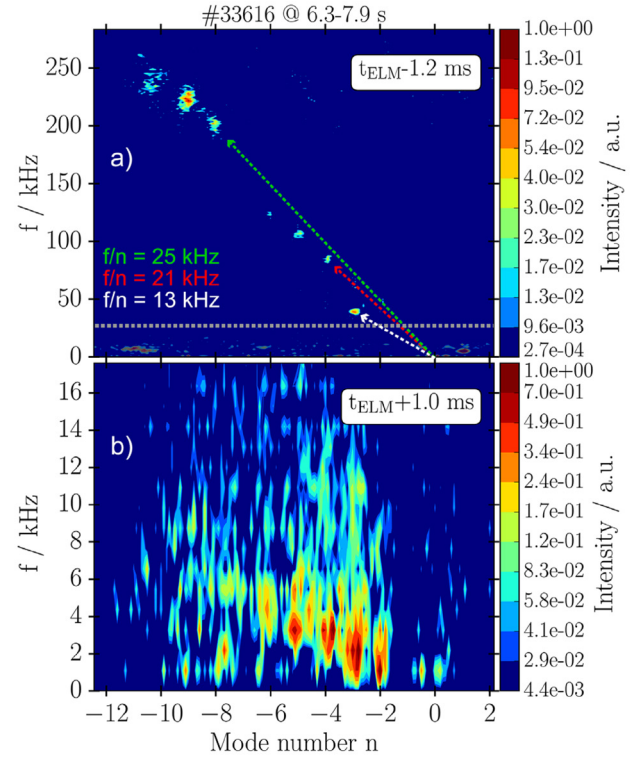
Figure 4. Frequency resolved mode number spectra of a time window (*a*) before and (*b*) during the type-I ELM crash. Reproduced courtesy of IAEA. Figure from [37]. © 2017 Max-Planck-Institut fur Plasmaphysik.

different localisation of the modes. The earlier clamping of ∇T_i and ∇n_e coincides with multi-harmonic lower n medium frequency (20 kHz $\lesssim f \lesssim$ 150 kHz) MHD activity. For an accurate localisation of the ECE emission through the pedestal radiation transport modelling is required [32]. The radiation transport model has been recently improved to allow for the oblique lines of sight of the ECE imaging [33] and also for third harmonic emission [34]. The improved edge measurements also allow to assess the ion heat transport during the ELM cycle [35]. The ion heat transport in H, D and He, modelled using ASTRA, was found to be close to NC. For the first time this was also done using the bulk ions in He discharges [36].

A novel mode analysis shows that during an ELM crash itself low n-modes are dominant, in good agreement with nonlinear resistive MHD modelling using JOREK [37, 38]. The JOREK modelling shows that the initially unstable higher n mode couples to low n-modes during the crash [39]. This can be seen in figure 4 showing the frequency resolved mode spectra (a) before and (b) during an ELM crash in the experiment. The low n sub-structure of the pre-ELM crash components appears with strongly reduced f/n (figure 4(*a*)) but similar dominant $n = 1, 2, 3, 4, 5$ during the crash (figure 4(*b*)). Another critical issue for future devices is the W transport by an ELM. This has now been modelled kinetically using JOREK [40]. The $E \times B$ drifts during the ELM lead to a radial transport of the impurities, which is in- and outwardly symmetrical in the radial direction. Such transport cannot be described by a 1D diffusive ansatz and would lead to a W
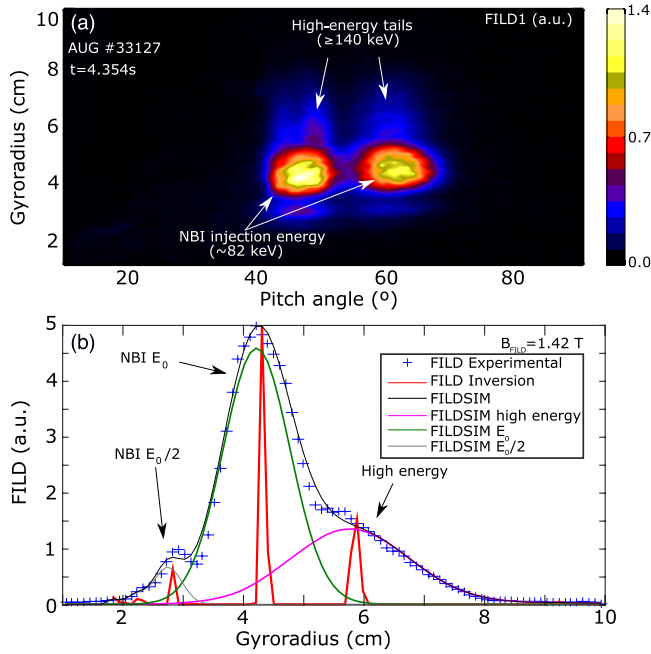
Figure 5. (*a*) Velocity space of fast-ion losses measured by a FILD during an ELM. (*b*) Gyroradius profile of the FILD signal. The blue crosses indicate the experimental FILD signal. In red, the undistorted gyroradius profile obtained after the tomographic inversion is plotted. The black curve is the expected gyroradius profile for the inverted distribution.

influx during the ELM in ITER as here hollow W density profiles are predicted.

The inward propagation of electron temperature perturbations induced by type-I ELMs has been analysed in a series of H-mode plasmas with moderate triangularity $\delta < 0.28$ [41]. It was found that the inward penetration of these perturbations mostly depends on the plasma current I_p or the edge saftey factor. The region affected by the ELMs extends deeper inside the confined region at lower I_p, in spite of the weaker ELMs. Estimates of the electron heat pulse diffusivity show that the transport is too large to be representative of the inter-ELM phase. This is in qualitative agreement with non-linear MHD simulations of an ELM done with JOREK [37, 38], which predicts an ergodization of the magnetic field lines during an ELM. The effective radial heat diffusion coefficient caused by the stochastic magnetic field perturbation calculated by JOREK [42] show a very similar radial profile compared to the experimental profile and are lower by a factor of two. Taking into account the convective transport as well, even better agreement would be achieved, however this detailed analysis has not yet been performed.

For the first time ion acceleration during the ELM has been measured [43] in plasmas with low density $\bar{n}_e \lesssim 6 \times 10^{19}$ m^{-3}, low pedestal collisionality $\nu^\star \lesssim 0.4$, $\beta_N \approx 2.5$, $I_p = 0.6 \cdots 1.0$ MA, $B_t = 1.8 \cdots 2.5$ T and $q_{95} = 3.7 \cdots 4.3$. In figure 5 data from the fast ion loss detector (FILD) during an ELM crash are shown. A high energy tail with energies $E_{acc} \geqslant 140$ keV above the NBI injection energy $E_0 = 82$ keV is evident in this NBI only heated discharge (see figure 5). The losses at the two different pitch angles observed in figure 5(*a*) originate from the
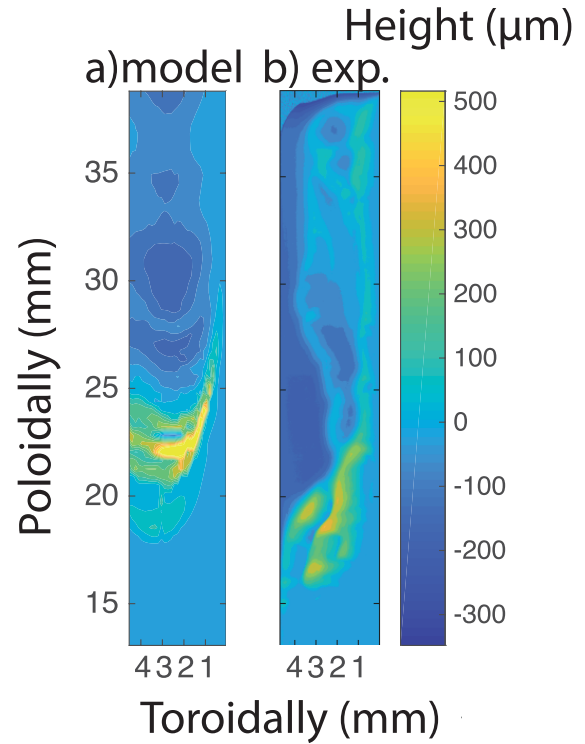
Figure 6. (*a*) Simulated final surface morphology profiles for the corrugated surface compared to (*b*) post-mortem measurements of the exposed surface [47].

use of two NBI sources with a more tangential (source 7) and radial (source 8) injection geometry. Inverting the data with respect to its instrument function reveals three sharp energy peaks at the gyroradii $\rho_L^{full} = 4.1$ cm, $\rho_L^{half} = 2.9$ cm and $\rho_L^{ELM} = 5.8$ cm e.g. in the gyroradius profile for the pitch angle $58° \leqslant \theta \leqslant 65°$ (figure 5(*b*) red line) corresponding to $E_0, E_0/2$ and ~160 keV respectively. The fast-ion loss happens temporally in sharp bursts indicating a filamentary behaviour. In order to explain the beam ion acceleration, the proposed mechanism is a resonant interaction between the beam ions and $E_\parallel$ generated during the ELM crash, when magnetic reconnection is believed to take place. Burst of microwave emission during the ELM may also be interpreted as evidence of high parallel electric fields during the ELM [44]. Such bursts were first observed on TFTR [45] but only later on MAST a connection to $E_\parallel$ inferred from JOREK simulations was reported [44]. Further evidence of reconnection during the ELM and the formation of an island is gained from analysing the growth of non-axisymmetric magnetic perturbations in discharges with an applied $n = 1$ magnetic perturbation field [46].

To better understand the potential target damage ELMs can cause the target heat loads and the thermionic emission current have been characterised with specially misaligned tiles [47, 48]. This has been used to benchmark modelling of the melt threshold and the melt motion using MEMOS 3D [49–51]. The melt layer motion is dominated by the $\vec{j}_{rep} \times \vec{B}$ force, where $\vec{j}_{rep}$ is the replacement current. $\vec{j}_{rep}$ is generated by the loss of electrons from the exposed surface due to the electron emission processes. MEMOS 3D has been modified to follow a self-consistent approach for the replacement current based
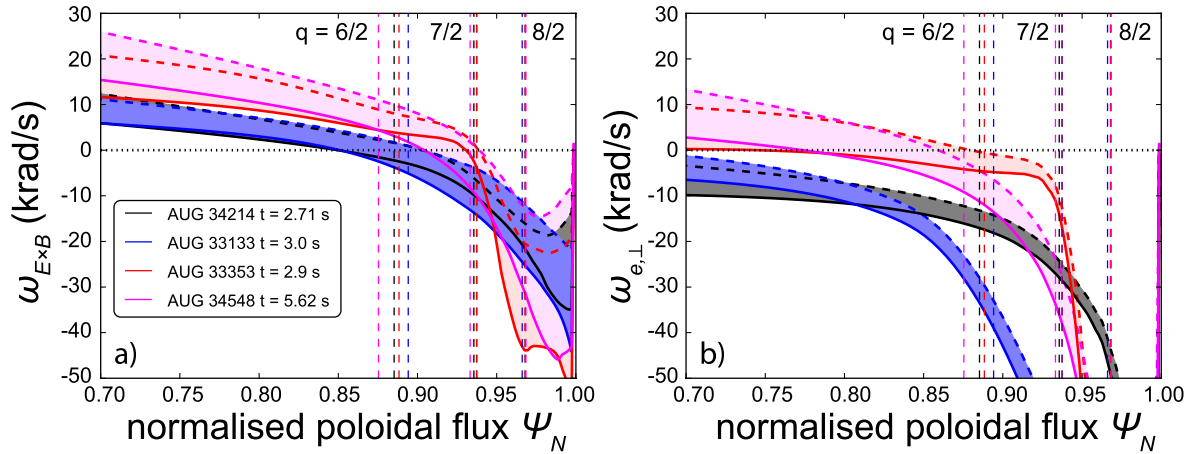
Figure 7. Profiles of angular rotation frequency of (*a*) gyrocenters ($E \times B$ flow) and (*b*) the electron fluid perpendicular to B for different discharges. The shaded regions indicate the confidence interval. The positions of various resonant surfaces are marked with vertical dashed line.

on the magnetostatic limit of the resistive thermoelectric MHD description of the liquid metal [50]. The escaping thermionic current depends on the plasma parameters as well as the B field and its inclination angle due to space charge formation and prompt redeposition effects [52]. To address this problem, dedicated particle-in-cell (PIC) simulations were carried out with the 2D3V SPICE2 code for the relevant inter and intra-ELM AUG parameters [53]. The PIC results revealed that the limited thermionic emission current exhibits a Child–Langmuir type scaling with the plasma parameters. This scaling has been translated into a dependence on the incident field-line parallel heat flux and employed in MEMOS modelling of the AUG sloped lamella melt experiment [51]. Figure 6 presents the simulated final surface morphology profile (b), to be compared with the experimental profile (a). The deformation structure is fairly well reproduced, with most of the displacement along the poloidal direction due to the $\vec{j}_{rep} \times \vec{B}$ force. The observed ridges in the exposed surface are attributed to the liquid build-up at the edge of the melt pool during individual melt events. Within the uncertainty of the experimental heat flux (about 25%), an agreement can be reached between modeled and observed total displaced melt volume within 10% error.

3. No ELM regimes and 3D perturbations

As the type-I ELM energy fluence to the divertor target scales $\varepsilon_{\parallel} \approx 6\pi p_{ped} \cdot R_{geo} \cdot q_{edge}$ [11], future devices likely need to avoid type-I ELMs altogether. A key technique to control ELMs is the excitation of a marginally stable kink-peeling response by an appropriately aligned (resonant) 3D magnetic perturbation field (RMP). Plasma response calculations with the linear resistive MHD code MARS-F and a free boundary 3D equilibrium solver VMEC version (NEMEC) can reproduce quantitatively the measured 3D displacements giving confidence in the accuracy of the models [54]. Using MARS-F, an analytic expression to predict the perturbation alignment in differential phase (field alignment) has been developed, which is accurate to about 30°. This analysis has also been applied to ITER equilibria [55].

At elevated triangularity ($\delta \sim 0.25$) ELM suppression is obtained on AUG at low, ITER like, pedestal collisionality [13, 56, 57]. Here good confinement of $H_{H98(y,2)} < 1.1$ is reached transiently and $H_{H98(y,2)} \lesssim 0.95$ stationarily depending on the perturbation strength. These normalised confinement factors are similar to those without 3D fields, albeit at lower n_e in the case with the RMP. $H_{H98(y,2)}$ can be somewhat optimised by reducing the applied perturbation field but so far it is not clear if that can be achieved on AUG with a stationary density. The AUG results suggest a more complicated physics picture to ELM suppression than previously reported, in particular with respect to plasma flows, collisionality and plasma response. Interestingly, the MARS-F plasma response calculations for a data base of RMP discharges with and without reaching ELM suppression show no clear difference of the kink-peeling response to differentiate between ELM suppression and ELM control [58]. For a fixed perturbation strength higher triangularity leads to a modest increased kink peeling response due to an increase of pedestal pressure. However, in the experiment the fixed coil currents lead to a decrease of the effective perturbation strength with increasing triangular as the distance of the plasma edge to the perturbation coils becomes larger.

JOREK calculations with perturbation currents above the experimentally achievable values suggest that it may be an enhanced tearing-kink response that leads to resonant plasma breaking $\omega_{e,\perp} \to 0$ and ELM suppression [59, 60]. In the modelling, the profile degradation by the applied error fields is not sufficient to explain the stabilisation of the peeling–ballooning modes, it only reduces their linear growth rates. Instead, non-linear mode coupling between the applied error field and the peeling–ballooning (p–b) modes leads to the saturation of the p–b modes [60, 61], which would still cause an ELM crash in the absence of the perturbation field at the same degraded pedestal profiles. A transition from a large ELM crash to a mitigated ELM crash and finally ELM suppression is observed when successively increasing the coil currents in the resonant error field configuration. At same coil currents, the non-resonant field configuration does not lead to ELM mitigation or suppression. In the modelled discharge,

the modes were still rotating in the ELM mitigation scenario while they were locked to the external error field in the ELM suppression simulation. This agrees with the general hypothesis for the access to ELM suppression where an island at the top of the pedestal forms if the perpendicular electron fluid $\omega_{e,\perp} \approx 0$ at a rational surface. From two fluid theory, this is believed to be necessary for the field to penetrate. However, the measurements show that ELM suppression can also be achieved with $\omega_{e,\perp} \neq 0$ over the full pedestal region. Whether suppression under these conditions can also be obtained in MHD simulations remains an open question.

In figure 7 the angular electron fluid rotation frequencies for various discharges are shown [57]. As can be seen from figure 7(b) the condition $\omega_{e,\perp} \approx 0$ close to a rational surface is not fulfilled for two of the four cases shown. For discharges #34214 (black) and #33133 (blue) a negative $\omega_{e,\perp} < 0$ is maintained over the whole pedestal within the uncertainties of the measurement. However, kinetic theory also shows resonances close to $\omega_{E \times B} \approx 0$, which is always given close to a rational surface near the edge (figure 7(a)). Whilst access to ELM suppression seems to be only possible under certain conditions the suppressed state has been maintained over a wider parameter range, suggesting that different physics may determine the density pump-out needed to access ELM suppression on AUG. In addition, ELM suppression has not been achieved at the lowest tested collisionalities, which may suggest a lower $\nu^\star$ limit or a pressure pedestal limit imposed by the (3D-reduced) ELM stability boundary [57].

Future devices will also need pellet fuelling. The compatibility of this fuelling method with RMP ELM control and suppression has been tested [62], extending previous studies of pellet and gas fuelling during ELM mitigation [63, 64]. In general, a strong correlation between the pedestal density and ELM energy loss (Spearman's correlation coefficient $r = 0.8$) is found from a database analysis of ELM control discharges including those with pellet fuelling [64]. Nevertheless, using a pellet rate of $\Phi_{pel} \approx 0.073 P_{aux}/T_i^{ped}$ (T_i^{ped}: ion temperature at the pedestal top) it was possible to restore the overall line integrated density, measured by an interferometer chord passing through the core, during the ELM control phase with still reduced ELM energy loss. In ELM suppressed scenarios at elevated triangularity, each pellet triggers ELM-like events but ELM suppression can be preserved in-between pellets, though not yet under stationary conditions. After a few pellets the plasma transited to an ELMy regime. As a low enough edge density or collisionality seems so far a necessary condition for ELM suppression [57] this is possibly related to the increase in edge density

A helically localised mode with ballooning structure (BM) has been observed as direct evidence for the modified local edge stability with MP [65]. In figure 8 the signature of the BM localised on a particular field line is evident from the radiation temperature measured with ECE during a rigid rotation of the perturbation field in time (figures 8(b) and (c)). The ECE channel at $f_{ECE} = 112.8$ GHz is shown corresponding to a poloidal radius averaged over one rotation period $\langle \rho_{pol} \rangle = 0.97$ in the steep gradient region. The measured
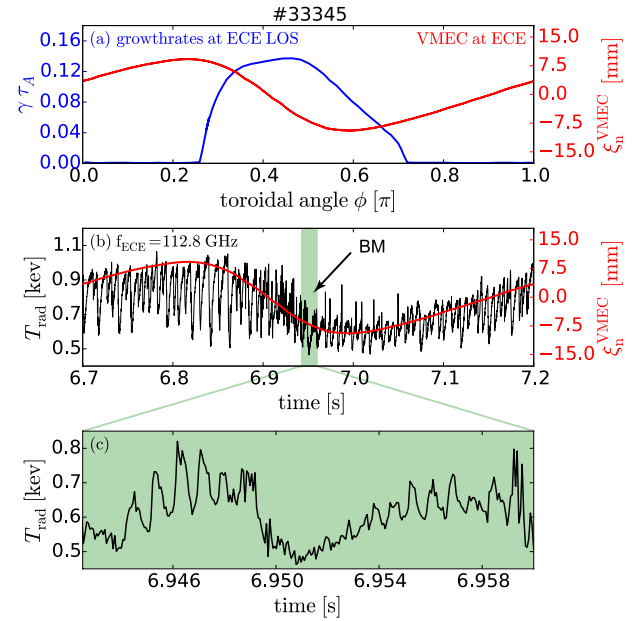
Figure 8. Evidence of helically localised ballooning modes during a rigid rotation of the RMP field in an ELMy H-mode (a) calculated growth rate on the most unstable field line (blue) as function of rotation angle. (b) ECE radiation temperature as function of time with the shaded time range magnified in (c). The calculated displacement of the perturbed equilibrium normal to the axisymmetric equilibrium, $\xi_n(\text{VMEC})$, from VMEC is shown in (a) and (b) in red.

corrugation compares well to the displacement of the 3D VMEC equilibrium normal to the axisymmetric equilibrium $\xi_n(\text{VMEC})$. Linear ideal ballooning theory shows a mode on the field line region that is least stable against field line bending due to the 3D corrugation [66, 67]. Measurements of T_e and n_e perturbations with a new fast He beam diagnostic [68] show neither a phase delay between T_e and n_e oscillation nor an inversion radius as expected for an island (see figure 9). Together, with the ECE measurement further inside also showing no inversion radius this confirms the ideal nature of the mode [67].

The alignment of the perturbation (set by the differential phase angle: $\Delta\phi_{ul}$) is also important for the fast-ion transport. Fast-ion losses at the edge can either be increased or decreased depending on the resonance with the bounce orbits (see section 5) [69]. The application of 3D perturbations results in a 2D lobe structure on the target heat load. Measuring the full heat load pattern using the rigidly rotating fields in L-mode show that the pattern toroidally averages to the unperturbed heat load profile on AUG and the toroidal variation decreases as the SOL density is increased [70–72]. In particular no local re-attachment is observed in detached regimes [73]. EMC3-EIRENE calculations with a simplified model for the plasma screening agree well with the measurements. The model only predicts a broadening of the heat flux profile due to RMPs for much narrower λ_q as expected on ITER [72, 74]. Furthermore, the 3D corrugation of the plasma also affects the coupling of ICRF heating [75]. A variation of the coupling resistance of $\Delta R_L \approx 20$ % has been measured in plasmas with
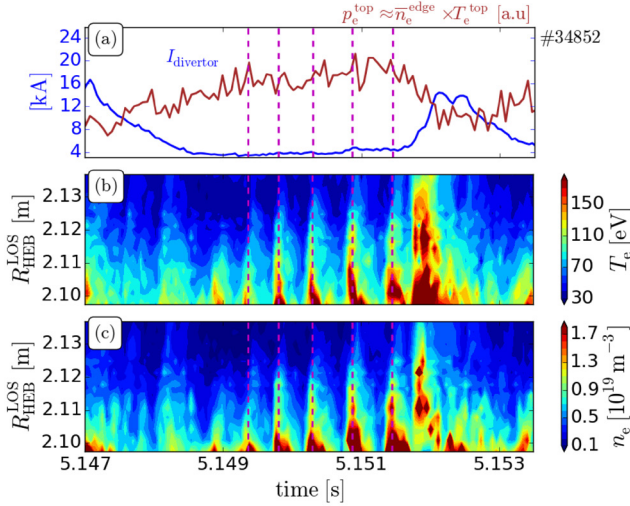
Figure 9. Evidence for the ideal mode structure from fast measurements with the new He beam diagnostic. (*a*) Divertor current (blue) as ELM signature and pedestal top pressure (red), (*b*) $T_e(R)$ and (*c*) $n_e(R)$ as function of time. Reproduced from [67]. © 2018 Max-Planck-Institut fur Plasmaphysik. CC BY 3.0.

Figure 10. Stationary I-mode with NBI feedback control on the value of β_{pol}. (*a*) NBI power, (*b*) pedestal top T_i and T_e (*c*) plasma energy, (*d*) β_{pol}, (*e*) line-average densities, (*f*) density fluctuation spectrogram at $\rho_{pol} = 0.99$. Reproduced from [79]. CC BY-NC-ND 4.0.

rigidly rotating $n = 2$ MP fields ($f = 6$ Hz, $I_B = 6.25$ kAt: current in in-vessel B-coil). This variation in coupling resistance can likely be attributed to the plasma displacement at the LFS mid-plane of a few mm as predicted by NEMEC calculations for $I_B = 5$ kAt. In addition, MHD modes, such as (2,1) NTMs, can also lead to variations of R_L.

Naturally ELM free high confinement scenarios such as the I-mode [76, 77] or QH-mode [35, 78], potentially attractive for DEMO, are also explored. For example, the operational regime for I-modes has been extended to $n/n_{GW} \leqslant 0.7$ in the open upper divertor. Using β feedback stationary I-modes with $n/n_{GW} \leqslant 0.58$ and $H_{98(y,2)} \sim 0.8$ have been achieved. An example for an I-mode discharge with β_{pol} feedback is shown in figure 10. β_{pol} is successively ramped up until an H-mode transition occurs. The reduction of NBI power due to the feedback recovers the I-mode interestingly at the same β_{pol} set-point that led to the I-H transition before. The power needed to access I-mode scales only weakly with the magnetic field $P_{LI} \propto B_t^{0.4}$ [77]. The average heat flux profile in I-mode is slightly narrower than in L-mode, but still broader than in H-mode [79]. However, intermittent fast density bursts have been observed that might be able to explain the L-mode like particle transport in I-mode, though a quantitative assessment is still pending. Each event consists of several bursts $\Delta t \approx 10$ μs clearly correlated to the weakly coherent mode (WCM). The WCM is apparent in T_e and n_e and its amplitude grows before the bursts and has now also been observed in the L-mode phase preceding the I-mode. These bursts also lead to a small dip in T_e and the measured temperature rise at the target is of the order of several 10 K. Owing to the short duration of these bursts this could correspond to very high parallel heat loads, that yet need to be characterised.

With respect to accessing QH-mode with a W wall, clear indications of the edge harmonic oscillation have been observed transiently [35] in co-NBI heated discharges. Following a recipe developed on DIII-D, the plasma rotation
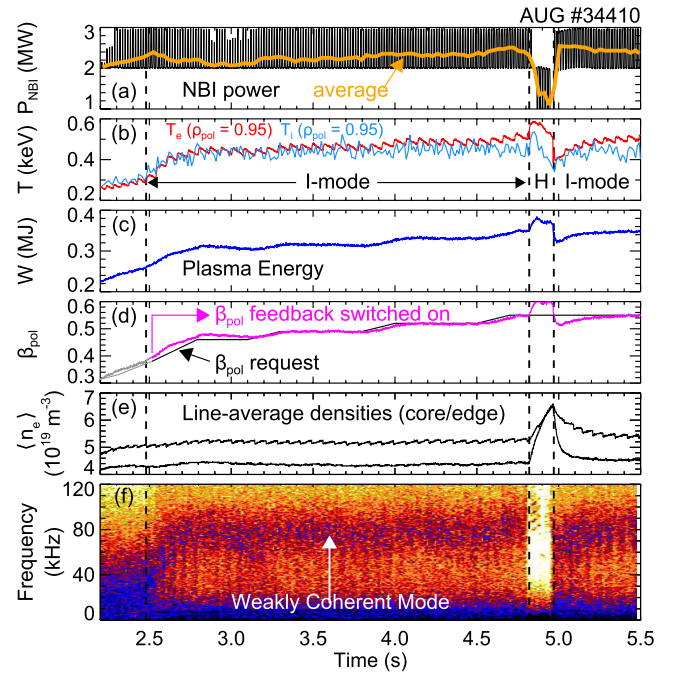
was increased before entering H-mode by strong NBI during an L-mode phase with the ion ∇B-drift away from the X-point and a subsequent down-shift of the plasma to enter H-mode at strong rotation. This leads indeed to a very deep E_r well with high shear thought to be crucial for accessing QH-mode. An effect on the density transport during the presence of the EHO is observed, but it is not strong enough to prevent the ELMs. Whilst QH mode was readily achieved on AUG with a C wall [80] this is the first time signs of the EHO have been seen with the W wall. Attempts are ongoing to develop a stationary QH-regime with a W wall and experiments with counter current NBI in reversed B_t/I_p are planned.

4. Scenarios and heating

The heating and current drive mix on AUG allows access to fully non-inductive MHD quiescent scenarios at $I_p = 0.8$ MA with $q_{95} = 5.5$, $\beta_N < 2.8$ and $H_{98(y,2)} \approx 1.1$ [2]. The plasma in this scenario is close to the 'no-wall' limit and small modification of the current profile as well as external perturbations become important [81]. These points are the subject of actual research for further scenario optimisations. A lower $I_p = 0.6$ MA variant of this non-inductive scenario ($q_{95} \approx 7.2$, $\beta_N = 2$, $H_{98(y,2)} \approx 0.85$) has been sustained for several current diffusion times showing that steady state can be achieved robustly [82]. At $I_p = 0.6$ MA the low confinement is due to the application of RMPs for n_e reduction. The modelling of $j(r)$ in these scenarios is in very good agreement with the measured profiles using no free parameters, thus proving predictive capability. This work has been aided by an improved equilibrium calculation taking the current diffusion
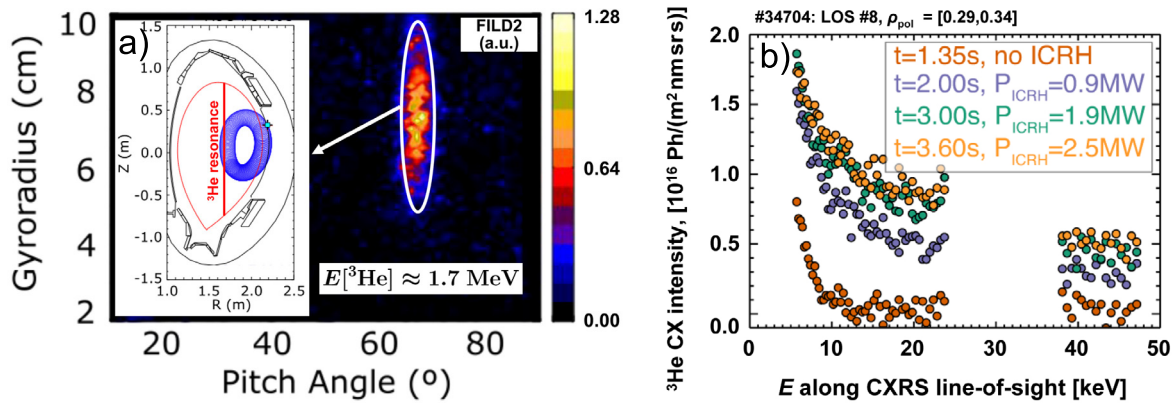
Figure 11. Three-ion H–^{3}He–D heating: (*a*) energy and pitch angle resolved fast-ion loss measured with FILD during on-axis heating, (*b*) energy spectrum of He ions from CXRS during off-axis heating at different ICRF powers.

into account [83, 84]. Here, also the understanding of radial fast-ion transport is important [85] (see section 5).

Work on the ITER base-line $Q = 10$ scenario (IBL) at $I_p = 1.2$ MA ($q_{95} = 3$, $\beta_N = 1.8$, $n/n_{GW} = 0.85$, $\delta = 0.4$ and $H_{H98(y,2)} = 1$) and its higher $q_{95} = 3.6$ at $I_p = 1.0$ MA ($\beta_N = 2.2$, $H_{H98(y,2)} = 1.2$) alternative (IBL-A) [86, 87] is ongoing with the aim to reach the required confinement by N_2 seeding and to reduce the ELM size using pellet pacing and RMPs. So far both high density scenarios still fall short of the required confinement by about 20% and ELM control techniques have a limited impact on the ELM frequency at $n/n_{GW} = 0.85$, though a slight density pump-out is observed with the application of RMPs. A high pressure in the divertor and a slightly lower average shear $\langle q' \rangle / \langle q \rangle$, however, lead to the onset of small ELMs (see section 2). Here, application of MP may also aid the transition to small ELMs. Most of the work in the past years has been done in the $q_{95} = 3.6$ IBL-A scenario. Here, seeding of N_2 reduces the HFSHD region but does not significantly improve the confinement. In contrast to studies at lower current and triangularity [14], which show a confinement improvement with N_2 seeding, in the IBL-A scenario the changes in the HFSHD region do not correlate with changes in the separatrix density. The performance of the IBL-A scenario was also tested using only ECRH and ICRH heating to dominantly heat the electrons and also reduce the torque input. No marked changes in perfomance have been observed. Operating at lower density trying to match $\nu^\star$ of ITER rather than n/n_{GW} leads to a higher confinement even in the presence of RMPs, which are used to lower n_e. For the IBL-A scenario $\nu^\star \approx 3\nu^\star_{ITER}$ has been achieved so far.

Scenario development is aided by more sophisticated control schemes, e.g. using a state observers based on the RAPTOR and RAPDENS codes [88]. This enables for example to maintain density control even if measurements become unavailable [89, 90]. Whilst switching between different density signals (e.g. interferometer and bremsstrahlung) the real time modelling of the density profile using RAPDENS can maintain plasma control even if the real-time density measurement is lost. Real-time temperature profile estimates from the RAPTOR state observer were used for feedback control of the electron temperature profile [91]. Using ECRH heating at different radial positions and varying the individual

power level accurate current drive studies with on- and off-axis NBI were facilitated [85]. The modular structure of the frame work allows easy implementation of additional modules. E.g. a module calculating the NBI fast-ion distribution in real time (RABBIT) has been developed and benchmarked with NUBEAM [92], which will improve the performance of the state observers in future. Work is ongoing to implement a path-oriented approach for disruption avoidance into this frame work as well. Such a path oriented approach has been demonstrated in feed forward by avoiding density limit disruptions [93] (see section 6).

Using feedback controlled pellet trains a plasma operating reliably at $n/n_{GW} \approx 1.2$ has been sustained [90]. Pellets have also been used to control the H to D ratio. The combined feedback of the core density, divertor pressure and strike-point electron temperature has been demonstrated using pellets, D_2 and N_2 gas puffs as actuators respectively [94]. This way the compatibility of the pellet fuelling with divertor detachment has been tested.

An improved understanding of the impact of ICRF power on the profile of electron density in the SOL n_e^{SOL} and the back reaction of the SOL on ICRF coupling has been gained using a set of reflectometer measurements inside the ICRF antenna [95] and retarding field energy analyser (RFEA) measurements on the field lines connecting to the antenna [96]. The measurements are in good qualitative agreement with self-consistent modelling of the oscillating E-fields (RAPLICASOL) and the sheath-rectified DC-fields (SSWICH) which induce $E \times B$ convection (EMC3-EIRENE) and modifications of n_e^{SOL} [97]. The impact of the three-strap antenna on the SOL density is smaller due to the lower DC-fields that also reduce W sputtering.

Following the experiments on JET and Alcator C-MOD [98] the three ion heating scheme using the ^{3}He resonance in H–D mixed plasmas has now been demonstrated on AUG as well [99]. Both on- and off-axis resonances were used with 30 MHz at $B_t = 3$ T and $B_t = 2.8$ T respectively. This heating scheme will likely enable ICRF heating on ITER in the non activation phase using a H–^{3}He–^{4}He mix. Peaked ion temperature profiles doubling the core T_i from $T_i = 2$ keV to $T_i > 4$ keV with the addition of $P_{ICRF} = 2.6$ MW on top of $P_{NBI} = 5$ MW (#34697) have been observed with the ^{3}He
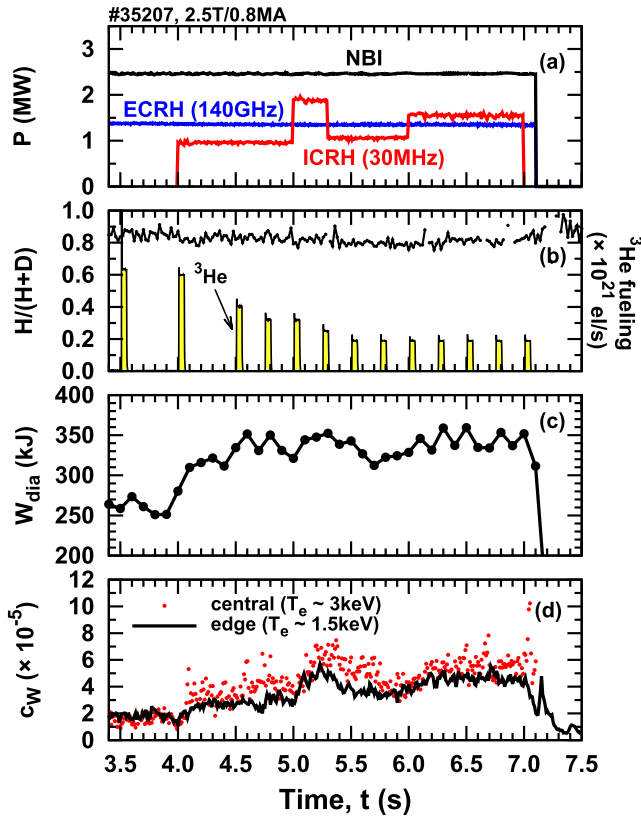
Figure 12. Overview of AUG pulse #35207 with far off-axis ICRH heating of ^{3}He ions in H D plasmas (2.5 T/0.8 MA): (*a*) NBI, ECRH and ICRH heating power; (*b*) H/(H + D) ratio measured by NPA and ^{3}He fuelling blips; (*c*) plasma stored energy; (*d*) tungsten concentration (core and edge).

resonance on-axis and 1%–1.5% ^{3}He concentration. The presence of multi-MeV He ions is evident from the large gyroradii detected in the FILD measurement shown in figure 11(*a*). The energetic He ions up-to 50 keV have been directly measured using CXRS [100] for the first time during three-ion heating and on AUG. The increase of the high energy tail between 10 keV $< E_{\text{He+}} <$ 50 keV during the ICRF application at different power levels is shown in figure 11(*b*).

In the next series of experiments on AUG, far off-axis three-ion ICRH heating scheme with ^{3}He in H–D mixture ($\rho_{\text{pol}} \approx 0.5$) at $B_t = 2.5$ T and its compatibility with avoiding core W accumulation in combination with core ECRH has been demonstrated (#35207, figure 12). This closely mimics the ITER heating scenario at 3–3.3 T in H–^{4}He mixed plasmas discussed in [101], in which off-axis ^{3}He heating ($f = 40$ MHz) has been proposed to facilitate achieving H-mode in hydrogen plasmas with ~10% of ^{4}He. The mix of heating systems on AUG (NBI, ECRH and ICRH) uniquely mimics the one of ITER, and further studies of such an integrated ITER-relevant scenario are foreseen on AUG.

5. Core fast-ion physics

A good confinement of the fast-ion population is of crucial importance towards the success of ITER and a future burning plasma. Fast-ions are, however, subject to transport by a rich

spectrum of electromagnetic perturbations such as Alfvén eigenmodes (AEs), ELMs, NTMs, sawteeth, etc. Some of them, such as weakly damped AEs, are expected to be unstable in ITER. A profound understanding and control of the fast-ion distribution and related electromagnetic perturbations is thus mandatory. In particular as the fast-ion distribution on ITER from the fusion born α-particles ($v_{i,\text{th}} \ll v_A \ll v_\alpha$) is isotropic a more complex non-linear interaction is predicted. Recently a scenario with off-axis NBI and accumulated W in the core creating a hollow T_e profile gave access to a large variety of energetic particle (EP) modes as can be seen in figure 13 [102]. In particular NBI driven steady toroidal Alfén eigenmodes (TAEs) during the current flat-top have not been accessible previously. For the first time on AUG this unique parameter space with $\beta_{\text{EP}}/\beta_{\text{th}} \approx 1$ and $E_{\text{EP}}/E_{\text{th}} \approx 100$ leading to non-linear coupling processes between the EP modes is accessible and can be diagnosed and modelled with the comprehensive set of tools available. For example velocity space tomography of the five different FI D$_\alpha$ spectra (FIDA) [103] has been used for the first time to infer the total D velocity distribution in NBI heated discharges showing a non-Maxwellian distribution function [104]. Evaluating the density, kinetic drift velocity and kinetic temperatures from the moments of the distribution function shows an anisotropic temperature with $T_\perp = 11$ keV $> T_\parallel = 9$ keV both substantially larger than the impurity temperature $T_{\text{B}^{5+}} = 7$ keV measured by CXRS. This is in excellent agreement with TRANSP calculations as can be seen from figure 14. Using this method also the fast-ion redistribution during a sawtooth crash has been studied showing clear discrepancies between the measurements and the TRANSP simulations [103].

The fast-ion transport and neutral beam current drive efficiency (NBCD) have been studied in discharges with elevated q-profiles, RMPs and edge-TAE activity. While good NBCD efficiency is obtained, strong losses of fast-ions with energies well below the injection energy are observed. These losses can, in part, be attributed to the RMP-induced error-fields, as modelled by VMEC and LOCUST. In addition, charge-exchange losses become strong during RMP operation (20% of the injected power) since the associated density-pump-out prolongs the fast-ion slowing down time such that the relative impact of charge-exchange losses increases. In contrast, a clear impact of the edge-TAEs on the fast-ion confinement could not be observed. If present, the level of the TAE-induced transport is below the modelling uncertainties of the fast-ion losses due to MPs and due to charge-exchange. The importance of the radial fast-ion transport has also been highlighted in a series of detailed NBCD studies with on- and off-axis NBI with feedback on the T_e profile [85]. Here, the on-axis case deviated from the NC predictions and both an ad hoc model of fishbone driven transport as well as turbulence driven transport led to good agreement between the FIDA measurements and the predictions from TRANSP modelling.

The effect of MPs on fast-ion losses has been studied in detail. The differential phase $\Delta\phi_{\text{ul}}$ between the upper and lower row of B-coils (alignment to the field) can be used to influence the fast-ion distribution [69]. The fast-ion transport and loss was analysed in terms of the canonical angular
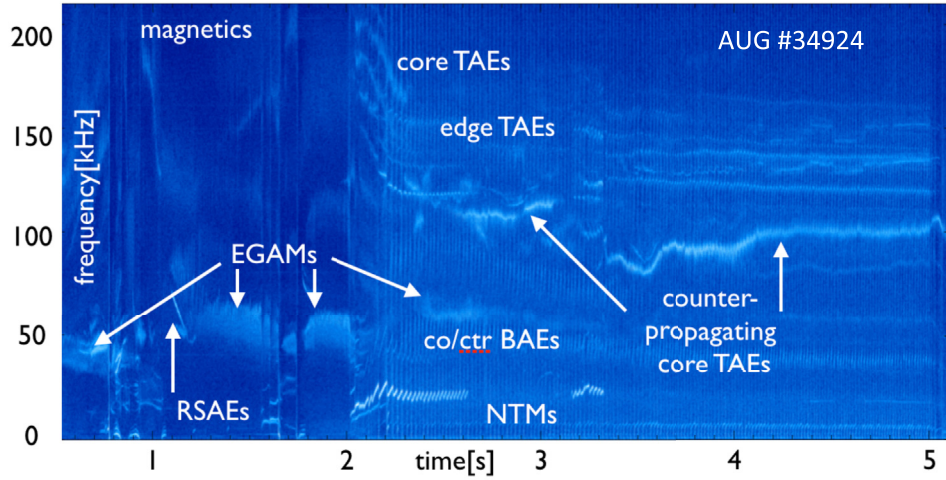
Figure 13. Magnetic spectrum of #34924 showing a variety of energetic particle driven modes in particular steady NBI driven TAEs during the flat-top previously not accessible on AUG.
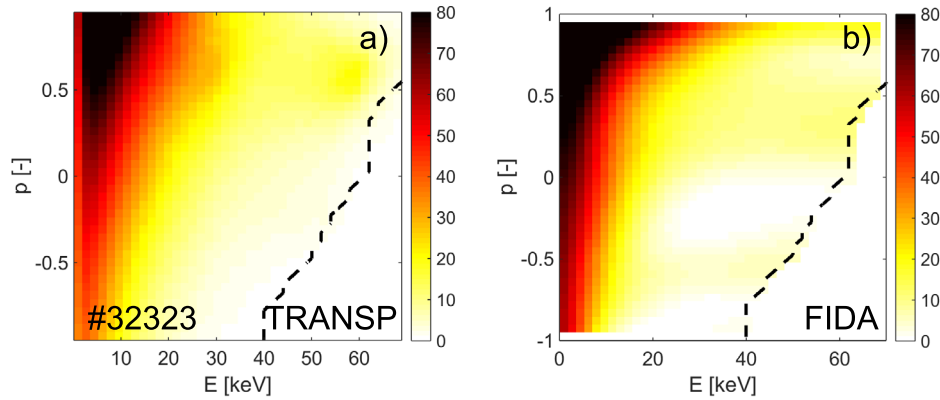
Figure 14. Deuterium distribution function in pitch-angle and energy from (*a*) TRANSP and (*b*) velocity space tomography of 5 FIDA views. Reproduced courtesy of IAEA. Figure from [104]. © 2018 EURATOM.

momentum $P_\phi = mRv_\phi - Ze\psi$. The combination of multiple linear and non-linear resonances creates an edge transport layer in the presence of the RMPs. Here, the structure of the perturbed angular momentum $\langle \delta P_\phi \rangle$ aligns well with geometrical orbital resonances of the bounce frequency divided by the average transit frequency $\omega_b/\bar{\omega}_d = n(l+1)/[p_0(l+1) \pm p']$ where n is the toroidal mode number of the perturbation, l the non-linear harmonic, $p = p_0 + p'$ the bounce harmonic with its primary, p_0, and additional, p', contribution. At different $\Delta\phi_{ul}$ different resonances are activated creating either inward transport or outward transport (see figure 15). The modelled and measured $\Delta\phi_{ul}$ dependence of the fast-ion loss are in good agreement if the plasma response is included and also the $n = 6$ side bands are considered. The RMP induced fast-ion loss may lead to high localised heat loads at the first wall and needs to be minimised together with the suppression of ELMs (see section 3).

This 'tailoring' of the fast-ion distribution at the plasma edge has also been used to demonstrate control of TAEs [105]. For this TAEs were excited ($B_t = 2.4$ T, $I_p = 0.8$ MA) during the flat-top by NBI in an optimised density range $n_e \approx (3.0 \cdots 4.5) \cdot 10^{19}$ m^{-3} and a monotonic elevated q-profile. Depending on the applied RMP alignment TAEs could be generated or suppressed. TAE and reversed shear AE (RSAE) control was also demonstrated using off-axis ECRH deposition [106]. Complete suppression of the RSAE was achieved during the ramp-up similar to earlier results on DIII-D [107]. However, in the presence of supra-Alfvénic ICRF accelerated ions TAEs were destabilised during the application of ECRH despite also leading to a 20% increase in n_e. SELFO calculations showed that with ECRH the FI slowing down time increases leading to a 40% higher FI stored energy and therefore a stronger TAE drive. Both, the effects of ECRH on RSAE and TAE result from changes in the profiles, which may not be applicable to ITER, but increase confidence in the FI modelling capability. The next step is to study the effect ECCD and first experiments have been performed recently.

6. Disruptions, runaway electrons and MHD

Disruptions are the single most dangerous abnormal plasma event in ITER and DEMO. To prevent damage to machine hardware their handling requires a multi stage approach: safe
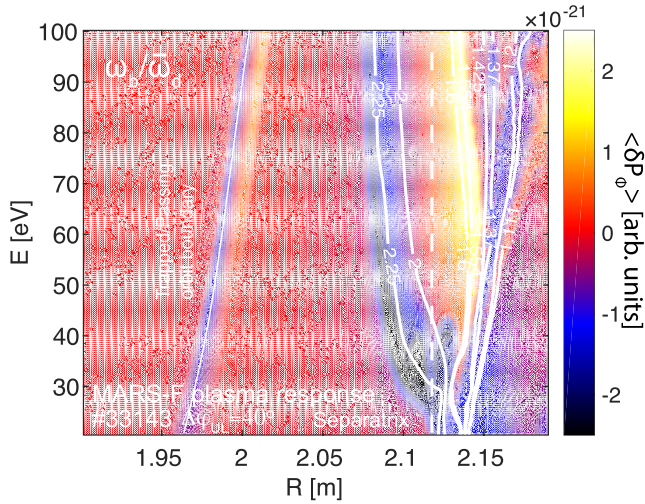
Figure 15. Perturbation of the canonical angular momentum by RMPs with overlayed geometrical resonances (lines). Blue areas correspond to inward transport and yellow areas to outward transport.
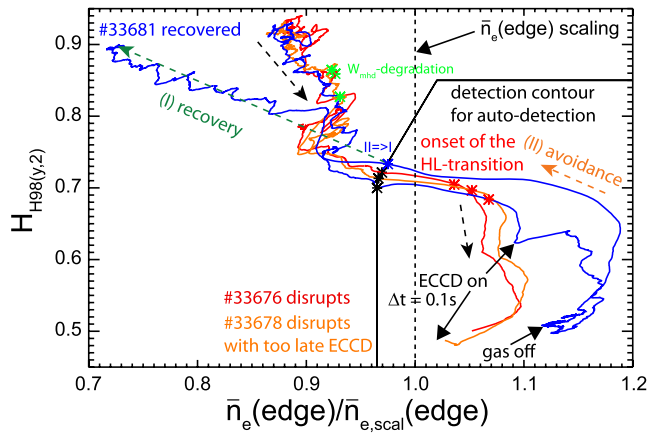
Figure 16. Different discharge trajectories of HDL discharges in ($\bar{n}_e^{edge}/\bar{n}_e^{scal}$, $H_{H98(y,2)}$) operational space together with a proposed detection contour. As avoidance schema ECCD at $q = 2$ is applied in feedforward and the gas fuelling is reduced. Three cases are shown: (red) no ECCD, (orange) ECCD applied too late and (blue) recovered discharge. Reproduced from [93]. © 2017 Max-Planck-Institut for Plasmaphysics.

Figure 17. Suppression of RE with the application of RMP as function of differential phase angle $\Delta\phi_{ul}$; (*a*) normalised radial field at the $q = 5$ surface from plasma response calculations with MARS-F; (*b*) generated RE current. Included are also discharges with different RMP amplitude (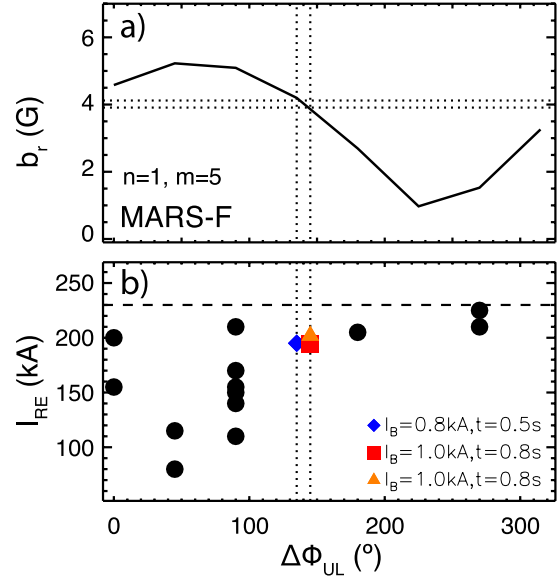B-coil current: I_B and timing (red square, orange triangle, blue diamond). Reproduced from [113]. © 2017 Universitá di Padova.

from disrupting until a safe density is reached. Rather than a trigger event a discharge state boundary is derived from a larger set of HDL disruptions using $H_{H98(y,2)}$ and the line averaged edge density $\bar{n}_e^{edge}$ measured with the DCN interferometer channel H-5 scaling like $\bar{n}_e^{scal} = 0.5 P_{heat}^{0.4} I_p^{0.3} q_{95}^{0.3}$ (P_{heat}: heating power). So far only the proof of principle has been demonstrated but application of this state boundary in the control system is planned for the upcoming campaign. In future more sophisticated machine independent state boundaries can be provided e.g. by a module in RAPTOR (see section 4). In parallel, in a Europe-wide effort including data from AUG, JET and TCV a tool is developed using generic descriptors to better identify the plasma states that are followed by disruptions in a machine independent way [109].

As a last resort the disruption has to be mitigated with respect to thermal and mechanical forces. On AUG disruption mitigation is provided using massive gas injection (MGI), whilst the ITER design uses mostly shattered pellet injection. The recent investigations have concentrated on finding the minimum gas (Ne) injection required to mitigate disruptions on AUG [110]. Forces and heat loads are mitigated with $N_{inj} > 10^{21}$ atoms of Ne. The pre thermal quench (TQ) phase has been modelled using the 1D ASTRA-STRAHL transport code recovering well the trends observed in the experiment validating it for the use on ITER [111]. The cooling of the $q = 2$ surface to below $T_e \lesssim 5$ eV is a good indicator for the TQ onset.

Mitigated and unmitigated disruptions are likely to generate runaway electrons (RE) in larger devices. Since 2014, an AUG runaway scenario has been accessed using an $n_e \approx 3 \times 10^{19}$ m^{-3}, $I_p = 0.8$ MA circular plasma disrupted by argon MGI [110]. The runaway beams have a typical

scenario control, disruption avoidance and recovery, controlled ramp down and as a last resort disruption mitigation. The different evolution a discharge can have towards a disruption (disruption path) will require a different strategy to handle the disruption [93, 108] (e.g. density limit versus β_N-limit disruptions). For each disruption path different sensors, triggers, actuators and algorithms may be required. These different handling strategies have been recently outlined on AUG and the handling of an H-mode density limit (HDL) discharge with this approach has been demonstrated [93]. It should be noted that generic disruption triggers (e.g. like MHD signatures) often are too quickly followed by a disruption for avoidance techniques to be employed. This is particularly the case for the HDL which can be avoided on AUG by ECCD at the $q = 2$ surface together with a reduction in fuelling (see figure 16). Here, the ECCD is used to prevent the discharge
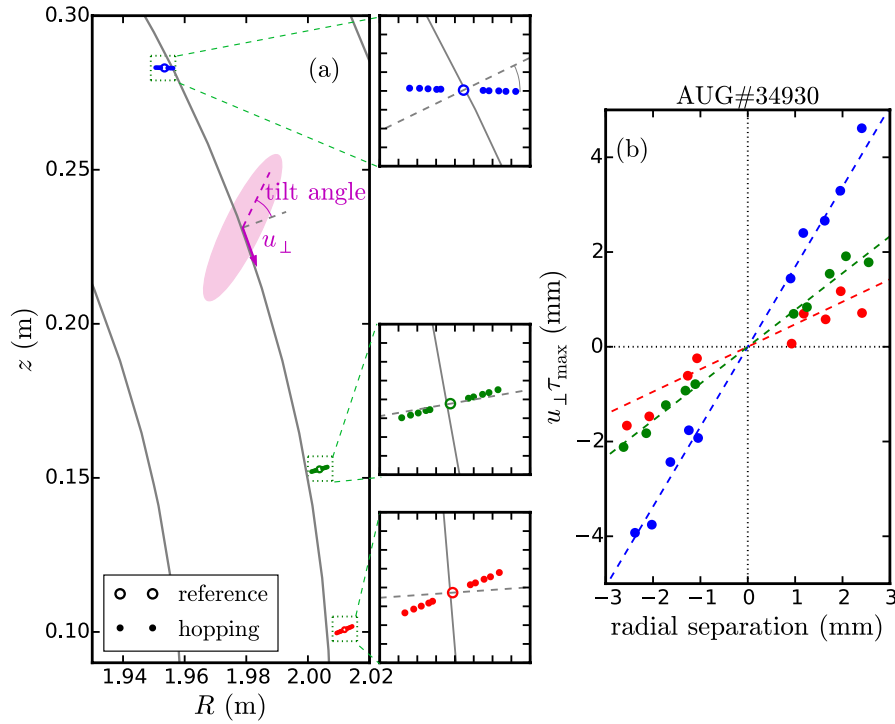
Figure 18. Eddy tilt angle: (*a*) measurement positions for three angles of incidence are shown on the AUG cross-section. The reference and hopping channels are depicted by squares and circles, respectively. Structures are artistically depicted. (*b*) The perpendicular offset $u_\perp \tau_{max}$ as a function of the radial displacement for the cases depicted in (*a*).

current of $I_{RE} = 0.2 \cdots 0.4$ MA and up to 0.5 s duration, allowing a large variety of RE studies, for example, RE dissipation by heavy impurities. AUG (and TCV) data show that the inclusion of full quantum mechanical treatment for the interaction of the relativistic electrons with the high Z material [112] improves the prediction of the RE dissipation. The application of carefully optimised $n = 1$ RMPs before the disruption creating a plasma response on the $q = 5$ surface has successfully prevented RE generation [113] in the standard RE scenario. This can be seen from figure 17 showing the generated RE current as function of the differential phase angle $\Delta\phi_{ul}$ between the upper and lower coil row. The application of the RMPs has led to a drop in energy and T_e by 30% before the disruption, and RE generation is expected to have a strong temperature dependence. However, when the effect of T_e before the disruption on the RE generation has been tested using ECRH heating, it revealed no clear trend as suggested by the RE generation theory. Modeling carried out with the GO code (a runaway fluid model coupled with atomic physics and background plasma evolution [114]) revealed that the nonlinear interplay between T_e and MGI assimilation rate and speed is hard to disentangle experimentally. The application of RMPs after the disruption showed no impact on the REs, but the conducting structures around the coils slow down the 3D field generation enough to hamper its effect. A fluid RE generation model has been implemented into JOREK [115] and has been successfully benchmarked against GO.

7. Transport

A deeper understanding of the plasma energy, particle and impurity transport has been gained by comparing detailed fluctuation and profile measurements with gyro-kinetic (GK) modelling. A strong constraint for turbulence modelling is for example the $n_e - T_e$ cross-phase angle α_{nT}. This has now been measured using correlation ECE [116] coupled to a reflectometer on the same line of sight giving simultaneously access to the T_e and n_e fluctuating fields [117]. Comparing these measurements with synthetic diagnostics of predicted GK (GENE) calculations at $\rho_{tor} = 0.75$ for an ECRH heated L-mode quantitative agreement is found with the ion heat flux Q_i, the electron heat flux Q_e, the radial correlation length of the T_e fluctuations $L_r(T_e)$ and α_{nT}, but the relative fluctuation level $\delta T_{e\perp}/T_e$ is consistently over-predicted. The reason for this discrepancy is still under investigation.

For the first time on AUG the eddy tilt angle of the density fluctuations has been measured with correlation Doppler reflectometry [118, 119]. The measurements for three poloidal positions are shown in figure 18. The vertical displacement computed from the perpendicular velocity $u_\perp$ and the time delay of the cross-correlation function τ_{max} shows clearly different slopes as function of radial separation indicating eddy tilting. The observed tilt angle changes in discharges where the heating mix is shifted towards dominant electron heating by replacing NBI with ECRH are most likely dominated by

changes in the $E \times B$ flow shear. In these experiments aimed to move from an ITG dominated to a TEM dominated turbulence regime the effect due to a change in $E \times B$ shear is stronger than the change in tilt angle expected from theory due to the change of turbulence state. GKW simulations indeed confirm that the growth rates and phase velocities correspond to a change from ITG to TEM dominated turbulence. Comparison of experimental and gyrokinetic results with linear ballooning theory shows that the $E \times B$ shear dominates the eddy tilt angle, in particular in the NBI phase [118, 119].

The change from TEM to ITG turbulence has also been considered the main reason behind the observed transition from linear (LOC) to saturated (SOC) Ohmic confinement with increasing density. Modelling with ASTRA and the TGLF model show that the turbulence transition is not required to obtain the confinement saturation [120]. This is correctly reproduced in the modelling by the increased electron and ion thermal coupling and the reduction of the impurity content with increasing density. The absence of a direct correspondence between the TEM to ITG turbulence transition and LOC-SOC transition is also confirmed by measurements of the phase velocity of the density fluctuations, comparing Doppler reflectometry measurements with $E \times B$ velocities measured by CXRS [121]. The poloidal velocity required to determine the $E \times B$ velocities are obtained through the difference between the HFS and LFS toroidal velocities. Thereby, while a turbulence transition from TEM to ITG is observed to take place with increasing density in both modelling and measurements, this is not related to the confinement mode transition and can take place before or after the LOC–SOC transition depending on plasma conditions. Furthermore, the CXRS measured poloidal rotation is observed to be in the ion diamagnetic direction around mid-radius, which is in the opposite direction with respect to the neoclassical predictions. The widely documented reversal of the intrinsic toroidal rotation in Ohmic plasmas has been simulated with both local [122] and global nonlinear GKW calculations [123]. The global profile shearing effect has been identified as the dominant symmetry breaking mechanism allowing the simulations to reproduce the measured levels of intrinsic rotation profile hollowness. The level of hollowness is strongly determined by the second derivative of the density profile in particular. All local mechanisms produce significantly weaker effects. An important role of TEM turbulence, this time destabilised by strong density gradients, has been found in gyrokinetic modelling of pellet fueled plasmas [124]. A new instability driven by reversed density gradients and leading to predominantly HFS turbulence is found in the GKW simulations and predicted to develop significant inward diffusion of passing particles at high collisionality. This instability is stabilized by a decrease of collisionality to the levels expected in a reactor plasma.

The impact of the main ion species on global plasma confinement is a key question for predicting DT operation in future power plants. Discharges run in H or He often show a degraded confinement with respect to D, which is normally not evident in GK simulations. The key role of the collisional electron–ion energy exchange has been highlighted experimentally in a study with matched L-mode plasmas in H and D [125]. The mass dependence of the collisional coupling is sufficient to explain the observed reduced confinement of the H plasma with respect to the D plasma, where the same temperature profiles are obtained with different heating powers. This result is supported by non-linear GK simulations with GENE of the stiff ion transport in ITG turbulence and related ASTRA modelling. In the ASTRA modelling the experimental observations for H and D are reproduced using a mass independent critical gradient model and the same transport coefficients [125]. The differences for H and D here are solely a consequence of the increased coupling between electrons and ions in H compared to D. No mass dependence of confinement is found in H-mode plasmas where the pedestal is matched through an increase of triangularity from D to H. The significance of the separate electron and ion heat transport channels has also been identified in a companion study dedicated to the understanding of the often observed reduced confinement in He plasmas with respect to D plasmas. Plasmas with matched conditions in He and D and with increasing fraction of electron heating show that the usual degradation is only observed in the presence of dominant ion heating, whereas in conditions of dominant electron heating He and D plasmas exhibit the same confinement. The degradation of confinement in conditions of dominant ion heating is consistent with the predicted reduction of zonal flows in electromagnetic ITG turbulence in He with respect to D in GKW simulations [126, 127].

An experimental quantification of the ion and electron transport stiffness is obtained by two sets of experiments with on- and off-axis NBI and on- and off-axis ECRH respectively. For the ions, the experimentally identified threshold agrees with the GK predictions and the expectations from stiff transport. This is in contrast to a recent interpretation reported on DIII-D [128]. On AUG the effect of fast-ion stabilization of ITG turbulence is clearly seen and identified by a comparison between experimental and GK modelling results. The electron heat transport experiments demonstrate a sudden significant increase of stiffness when R/L_{T_e} exceeds 6 around mid-radius, with a heat pulse conductivity which suddenly exceeds the power balance conductivity. This is consistent with the GK predicted destabilization of ETG modes. The importance of separately reproducing the ion and electron heat fluxes in plasmas which aim at reproducing the conditions in a burning plasma has been highlighted in a set of experiments in which also the torque and particle sources have been matched to those expected in a reactor [129]. In addition, the experimental results show the dominant role of the inward convection with respect to the particle source in determining the density peaking in these conditions. Theory-based modelling predicts a reduction of the density peaking with increasing β.

The impact of different fractions of electron to ion heating has also been studied in the framework of impurity transport. For this study a new ICRF modulation technique has been developed and exploited at AUG to separately determine both the diffusion and the convection profiles of boron [130] (see figure 19). In contrast to heavy impurities like W, whose behavior in AUG is correctly predicted by the combination of neoclassical and GK models [131], light impurities, whose
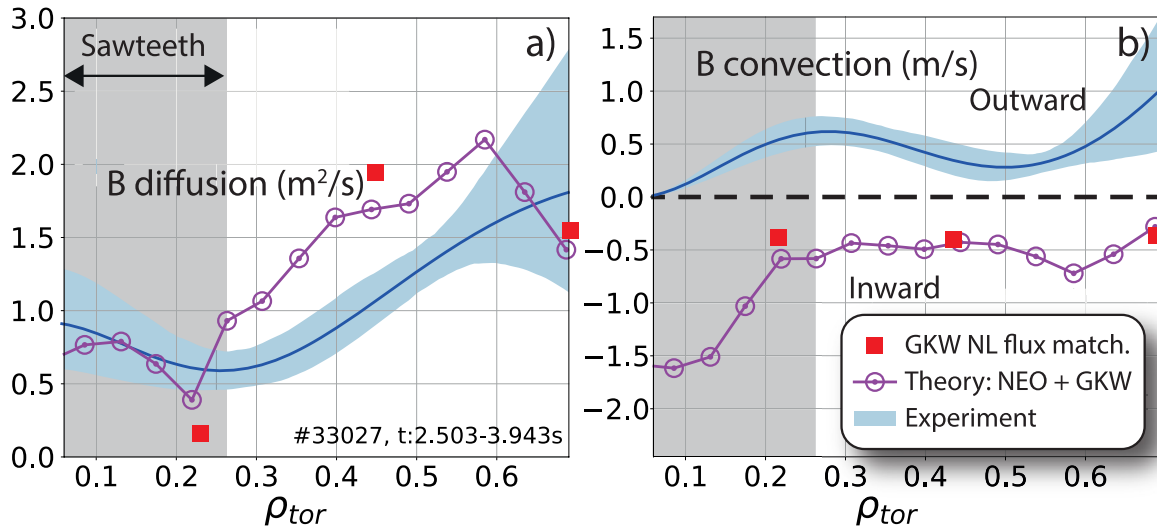
Figure 19. Comparison of (blue) measured radial profiles of the Boron transport coefficients with coefficients form (purple, circle) neocl. plus quasi-linear GKW modelling and (red, squars) flux matched nonlinear GKW modelling. Shown are (*a*) the diffusion coefficient and (*b*) the convection velocity. Reproduced from [130]. © IOP Publishing Ltd. CC BY 3.0.
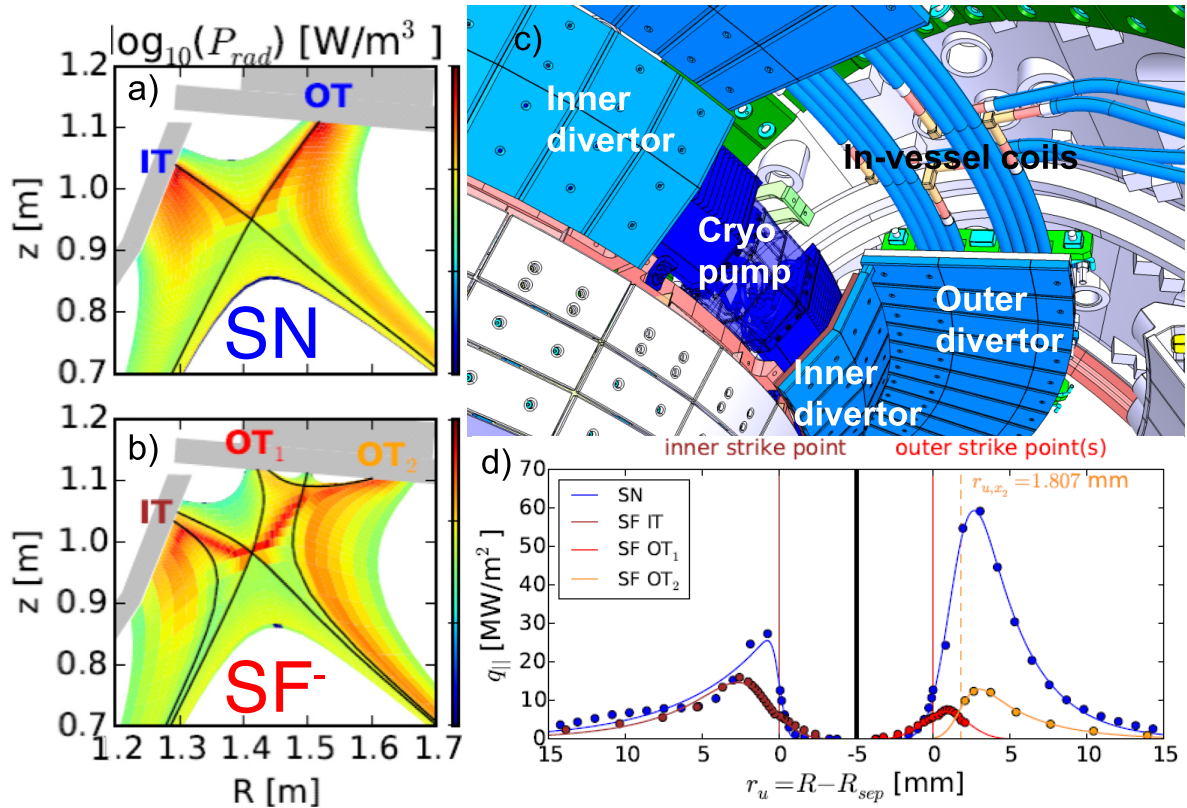
Figure 20. New upper divertor: contours of P_{rad} from SOLPS in (*a*) single null (SN) and (*b*) LFS snow-flake (SF$^-$) configuration, (*c*) current design and (*d*) predicted target heat loads for different configurations from SOLPS. Reproduced from [135]. © IOP Publishing Ltd. CC BY 3.0.

transport is dominated by turbulence in both the diffusive and the convective components, are not correctly predicted by current theoretical models. The comparison between the results from ICRF modulation experiments and the GKW predictions reveal that while the diffusivity of B is reasonably well reproduced under most conditions (figure 19(*a*)), the observed outward convection in conditions of dominant NBI heating is not reproduced by the modelling, which

predicts an impurity pinch for both dominant ion and electron heating (figure 19(*b*)). These results are consistent with the recently documented deficiencies of current turbulent transport models in completely reproducing the behavior of the density profiles of He and B in AUG [132]. This is in particular true for hollow impurity density profiles, and demonstrates that the disagreement with theory is predominantly in the convective components.

18

8. Summary and outlook

The combined domestic and European programme on AUG has considerably improved the physics basis for ITER and DEMO during the last two years. Fundamental to this has been the direct, detailed comparison between theory, simulation and experiment facilitated by better diagnostics, novel analysis techniques and significant code developments. Improved tile design and clamping has alleviated the previously encountered cracking in the bulk W tiles. Advances in heating capabilities and control have enabled access to better scenarios. The upgraded power supplies for the in-vessel B-coils have allowed more sophisticated studies with 3D magnetic perturbations (MP) and the MP fields are now also used to enable new low collisionality scenarios. Key highlights of the programme are the deeper understanding of the edge localised mode (ELM) stability, crash dynamics and impacts on plasma facing components, the insight into 3D physics for ELM suppression and fast-ion confinement as well as the detailed comparison between turbulence characteristics and gyro-kinetic modelling.

The ELM crash and pedestal recovery have been measured with unprecedented accuracy in D, H and He and MHD modes have been identified that coincide with the clamping of density and temperature profiles. Evidence of reconnection during the ELM crash is given by the acceleration of ions detected with the fast-ion loss detector as well as magnetic measurements. The W melt motion for misaligned targets has been characterised in detail including measurements of the thermionic emission currents, which has led to important enhancements of the melt motion modelling with respect to the replacement currents.

To mitigate the impact of ELMs on the targets ELM control via RMPs is studied and the kink peeling plasma response is found to be instrumental for the control. The non-linear and linear resistive MHD modelling of the edge displacement by the plasma response during the application of MPs is in excellent agreement with the measured 3D displacement giving further credence to the codes. The operational space for full ELM suppression has been widened and scenarios with good confinement have been achieved by fine tuning the perturbation field. Here, the operational window to maintain ELM suppression is found to be larger than the access window. Access to ELM suppression is to a large extent determined by the density pump-out. ELM suppression has been attained with a wide variation of the edge rotation questioning the common picture requiring a vanishing perpendicular electron flow close to rational surfaces to facilitate field penetration and the formation of an island at the pedestal top. Direct evidence for the altered edge stability in the presence of a MP has been found with the observation of a helically localised ballooning mode. The mode is destabilised on a single bad curvature line and its localisation is in good agreement with growth rates predicted by theory.

Ballooning modes, this time destabilised close to the separatrix, may also be key to the H-mode density limit and are a good candidate for the small ELMs observed at high separatrix density and strong shaping. These small ELMs combine good confinement with an ITER like SOL. In particular the high density manifestation of the AUG ITER base-line scenario and its higher $q_{95} = 3.6$ derivative are found to be close to the threshold for small ELMs. Furthermore, the $q_{95} = 3.6$ variant has now been extended to pure wave heating with dominant electron heating and low rotation as well as low collisionality only a factor of two to three above the ITER value. The latter is facilitated by density pump-out using MPs. Whilst the high density scenario has still too low confinement at the required normalised pressure the confinement of the low collisionality variant is found to be sufficient. Validating heating methods for ITER, such as a novel three ion ICRF heating scheme previously explored at CMOD and JET has now been successfully adapted on AUG. Efficient ion heating with the ^{3}He resonance on-axis and 1%–1.5% ^{3}He concentration could be demonstrated. This heating scenario is expected to facilitates ICRF heating during the non-active phase on ITER in hydrogen (H) plasmas.

Operation without ELMs will likely be crucial for DEMO. Apart from ELM suppression by MPs the I-mode scenario has been further developed and first attempts on recovering QH-mode with a W wall have been started. Stationary I-mode on AUG has been achieved with 60% of the Greenwald density (n_{GW}) and $H_{H98(y,2)} = 0.8$. Transiently $n/n_{GW} = 0.7$ has been reached. The heat flux width is found to be in between L- and H-mode, but fast, transient intermittent density bursts have been observed that might lead to a high target heat flux.

A better characterisation of the current drive modelling in non-inductive scenarios has given confidence in the predictive capability, but also highlighted the importance of radial fast-ion redistribution. Here, a good reconstruction of the velocity distribution of the confined fast-ions has been achieved using velocity space tomography of the various fast-ion D_α measurements. In addition, the fast-ion losses have been studied using multiple fast-ion loss detectors. The special focus of these studies has been the fast-ion loss due to MPs showing a good alignment of the orbital resonances with changes in the canonical angular momentum. A better understanding of energetic particle modes has been gained by accessing a new scenario with $\beta_{EP}/\beta_{th} \approx 1$ and $E_{EP}/E_{th} \approx 100$ and also by modifying TAE and RSAE stability with RMPs and via profile changes using ECRH. The accurate modelling of this activity gives confidence in the predictions of burning plasmas.

With respect to core energy, momentum and particle transport new measurements such as the $n_e - T_e$ cross phase or the eddy tilt angle allow a benchmark of gyro-kinetic (GK) simulations to a much deeper level than previously possible. The changes in the eddy tilt angle observed with different heating schemes to access ITG and TEM dominated regimes are so far dominated by the change in $E \times B$ flow shear as expected changes due to the turbulence state derived from GK simulations are small. Poloidal flow profiles, determined from LFS-HFS asymmetries of the toroidal flows, supported by GK modelling indicate that in Ohmic discharges a transition from TEM to ITG turbulence occurs. This transition, however, is not related to the transition between linear and saturated Ohmic confinement as previously stated.

The key role of the collisional electron–ion energy exchange has been elucidated in a series of experiments, being sufficient to explain the differences in core transport observed in H, D and He L-mode discharges. The reduction of zonal flows in electromagnetic ITG turbulence in He in comparison to D seen in GK simulations is consistent with the degradation of confinement in the presence of dominant ion heating. GK simulations also agree with the experimentally identified threshold for stiff ion transport and predict a destabilisation of ETG when experimentally a sudden increase in the T_e profile stiffness is observed at mid-radius. With respect to impurity transport, discrepancies between modelling and experiments are still found for light species such as B and He.

AUG is currently embarking on a substantial enhancement of the upper divertor co-funded by EUROfusion [133, 134]. The new upper divertor (see figure 20(c)) is in its final design stage and will be implemented during a long shutdown starting 2021. The aim is to allow access to different alternative divertor configurations in the upper divertor by implementing two in-vessel wound poloidal field coils as well as a cryogenic pump and a suite of diagnostics to fully characterise the new divertor. This will facilitate studies of these configurations with high P/R. In preparation of this enhancement experiments characterising the upper divertor in its current state are ongoing to develop the required modelling capability. First modelling for the new upper divertor is shown in figure 20 [135] comparing an upper single null divertor configuration (SN, figure 20(a)) with a near snow flake configuration, were the additional X-point is in the outer SOL (SF⁻: figure 20(b)). The modelling predicts a stronger radiation in SF⁻ and a factor of four reduction in heat flux density under similar up-stream conditions (figure 20(d)). In addition to the upper divertor a Thomson scattering system in the lower divertor (also co-funded by EUROfusion) comes online in early 2019. Also for 2019 an imaging heavy ion beam is planned to probe density and plasma potential at the plasma edge. These enhancements will further strengthen the key role ASDEX Upgrade plays on the path to a future fusion power plant.

Acknowledgments

References

[1] Neu R. *et al* 2007 *Plasma Phys. Control. Fusion* **49** B59
[2] Bock A. *et al* 2017 *Nucl. Fusion* **57** 126041
[3] Wagner D. *et al* 2017 *EPJ Web Conf.* **149** 03004
[4] Teschke M. *et al* 2017 *Fusion Eng. Des.* **124** 141
[5] Herrmann A. *et al* 2017 *Nucl. Mater. Energy* **12** 205
[6] Zammuto I. *et al* 2017 *Fusion Eng. Des.* **124** 297
[7] Neu R. *et al* 2017 *Fusion Eng. Des.* **124** 450
[8] Zammuto I. *et al* 2018 *Fusion Eng. Des.* **136** 1052
[9] Neu R. *et al* 2018 *J. Nucl. Mater.* **511** 567
[10] Wolfrum E. *et al* 2017 *Nucl. Mater. Energy* **12** 18
[11] Eich T. *et al* 2017 *Nucl. Mater. Energy* **12** 84
[12] Sieglin B. *et al* 2017 *Phys. Scr.* **2017** 014071
[13] Meyer H. *et al* 2017 *Nucl. Fusion* **57** 102014
[14] Dunne M.G. *et al* 2017 *Plasma Phys. Control. Fusion* **59** 014017
[15] Dunne M.G. *et al* 2017 *Plasma Phys. Control. Fusion* **59** 025010
[16] Frassinetti L. *et al* 2017 *Nucl. Fusion* **57** 022004
[17] Guimarais L. *et al* 2018 *Nucl. Fusion* **58** 026005
[18] Reimold F. *et al* 2017 *Nucl. Mater. Energy* **12** 193
[19] Eich T. *et al* 2018 *Nucl. Fusion* **58** 034001
[20] Harrer G. *et al* 2018 *Nucl. Fusion* **58** 112001
[21] Kallenbach A. *et al* 2018 *Plasma Phys. Control. Fusion* **60** 045006
[22] Vianello N. *et al* 2018 SOL transport and filamentary dynamics in high density tokamak regimes *Preprint: 2018 IAEA Fusion Energy Conf. (Gandhinagar, India, 22–27 October 2018)* [EX/P8-13]
[23] Carralero D. *et al* 2018 *Nucl. Fusion* **58** 096015
[24] Allan S.Y. *et al* 2016 *Plasma Phys. Control. Fusion* **58** 045014
[25] Drenik A. *et al* 2018 *23rd Conf. on Plasma Surface Interactions PSI-23 (Princeton, NJ, USA, 17–22 June 2018)* (http://hdl.handle.net/21.11116/0000-0001-6F57-2)
[26] Drenik A. *et al* 2019 *Nucl. Fusion* **59** 046010
[27] Sun H.J. *et al* 2017 *Plasma Phys. Control. Fusion* **59** 105010
[28] Sun H.J. *et al* 2019 *Plasma Phys. Control. Fusion* **61** 014005
[29] Cavedon M. *et al* 2017 *Plasma Phys. Control. Fusion* **59** 105007
[30] Laggner F.M. *et al* 2017 *Phys. Plasmas* **24** 056105
[31] Vanovac B. *et al* 2018 *Nucl. Fusion* **58** 112011
[32] Rathgeber S.K. *et al* 2013 *Plasma Phys. Control. Fusion* **55** 025004
[33] Denk S.S. *et al* 2017 *EPJ Web Conf.* 147 02002
[34] Denk S.S. *et al* 2018 *Plasma Phys. Control. Fusion* **60** 105010
[35] Viezzer E. *et al* 2018 *Nucl. Fusion* **58** 026031
[36] Viezzer E. *et al* 2018 ELM-induced energy and momentum transport in ASDEX Upgrade *Preprint: 2018 IAEA Fusion Energy Conf. (Gandhinagar, India, 22–27 October 2018)* [EX/P8-5]
[37] Mink A. *et al* 2018 *Nucl. Fusion* **58** 026011
[38] Hoelzl M. *et al* 2018 *Contrib. Plasma Phys.* **58** 518
[39] Krebs I. *et al* 2013 *Phys. Plasmas* **20** 082506
[40] Van Vugt D. *et al* 2019 *Phys. Plasmas* **26** 042508
[41] Trier E. *et al* 2019 *Plasma Phys. Contr. Fusion* **61** 045003
[42] Rechester A.B. *et al* 1978 *Phys. Rev. Lett.* **40** 38
[43] Galdon-Quiroga J. *et al* 2018 *Phys. Rev. Lett.* **121** 025002
[44] Freethy S.J. *et al* 2015 *Phys. Rev. Lett.* **114** 125004
[45] Taylor G. *et al* 1992 *Nucl. Fusion* **32** 1867
[46] Wang N. *et al* 2019 *Nucl. Fusion* **59** 054002
[47] Krieger K. *et al* 2018 *Nucl. Fusion* **58** 026024
[48] Krieger K. *et al* 2017 *Phys. Scr.* **2017** 014030
[49] Thorén E. *et al* 2017 *Phys. Scr.* **2017** 014006
[50] Thorén E. *et al* 2018 *Nucl. Fusion* **58** 106003
[51] Thorén E. *et al* 2018 *Nucl. Mater. Energy* **17** 194
[52] Komm M. *et al* 2017 *Plasma Phys. Control. Fusion* **59** 094002
[53] Komm M. *et al* 2017 *Phys. Scr.* **2017** 014069
[54] Willensdorfer M. *et al* 2017 *Nucl. Fusion* **57** 116047
[55] Ryan D.A. *et al* 2018 *Plasma Phys. Control. Fusion* **60** 065005
[56] Suttrop W. *et al* 2017 *Plasma Phys. Control. Fusion* **59** 014049
[57] Suttrop W. *et al* 2018 *Nucl. Fusion* **58** 096031
[58] Ryan D. *et al* 2019 *Plasma Phys. Control. Fusion* accepted (https://doi.org/10.1088/1361-6587/ab32fa)
[59] Orain F. *et al* 2017 *Nucl. Fusion* **57** 022013
[60] Orain F. *et al* 2019 *Phys. Plasmas* **26** 042503
[61] Bécoulet M. *et al* 2014 *Phys. Rev. Lett.* **113** 115001

[62] Valovič M. *et al* 2018 *Plasma Phys. Control. Fusion* **60** 085013
[63] Valovič M. *et al* 2016 *Nucl. Fusion* **56** 066009
[64] Leuthold N. *et al* 2017 *Plasma Phys. Control. Fusion* **59** 055004
[65] Willensdorfer M. *et al* 2017 *Phys. Rev. Lett.* **119** 085002
[66] Cote T.B. *et al* 2019 *Nucl. Fusion* **59** 016015
[67] Willensdorfer M. *et al* 2019 *Plasma Phys. Control. Fusion* **61** 014019
[68] Griener M. *et al* 2018 *Rev. Sci. Instrum.* **89** 10D102
[69] Sanchis L. *et al* 2019 *Plasma Phys. Control. Fusion* **61** 014038
[70] Faitsch M. *et al* 2017 *Nucl. Mater. Energy* **12** 1020
[71] Faitsch M. *et al* 2017 *Plasma Phys. Control. Fusion* **59** 095006
[72] Faitsch M. *et al* 2019 *Plasma Phys. Control. Fusion* **61** 014008
[73] Brida D. *et al* 2017 *Nucl. Fusion* **57** 116006
[74] Brida D. *et al* 2018 *23rd Conf. on Plasma Surface Interactions PSI-23 (Princeton, NJ, USA, 17–22 June 2018)* (https://psi2018.princeton.edu)
[75] Suárez López G. *et al* 2017 *EPJ Web Conf.* **157** 03051
[76] Hubbard A. *et al* 2016 *Nucl. Fusion* **56** 086003
[77] Happel T. *et al* 2017 *Plasma Phys. Control. Fusion* **59** 014004
[78] Burrell K.H. *et al* 2002 *Plasma Phys. Control. Fusion* **44** A253
[79] Hvappel T. *et al* 2019 *Nucl. Mater. Energy* **18** 159
[80] Suttrop W. *et al* 2005 *Nucl. Fusion* **45** 721
[81] Igochine V. *et al* 2017 *Nucl. Fusion* **57** 116027
[82] Bock A. *et al* 2018 *Phys. Plasmas* **25** 056115
[83] Fischer R. *et al* 2016 *Fusion Sci. Technol.* **69** 526
[84] Fischer R. 2017 *Europhysics Conf. Abstracts (CD-ROM, Proc. of the 44th EPS Conf. on Plasma Physics (Belfast, Northern Ireland (UK), 26–30 June 2017))* (*ECA* vol 41F) ed M. Fajardo *et al* (Geneva: European Physical Society) p P4.133 (http://ocs.ciemat.es/EPS2017PAP/pdf/P4.133.pdf)
[85] Rittich D. *et al* 2018 Quantification neutral beam driven current and the effect of radial fast ion redistribution in ASDEX Upgrade *Preprint: 2018 IAEA Fusion Energy Conf. (Gandhinagar, India, 22–27 October 2018)* [EX/P8-25]
[86] Schweinzer J. *et al* 2016 *Nucl. Fusion* **56** 106007
[87] Pütterich T. *et al* 2018 The ITER baseline scenario investigated at ASDEX Upgrade *Preprint: 2018 IAEA Fusion Energy Conf. (Gandhinagar, India, 22–27 October 2018)* [EX/P8-4]
[88] Felici F. 2017 *Europhysics Conf. Abstracts (CD-ROM, Proc. of the 44th EPS Conf. on Plasma Physics (Belfast, Northern Ireland, UK, 26–30 June 2017))* (*ECA* vol 41F) ed M. Fajardo *et al* (Geneva: European Physical Society) p P1.151 (http://ocs.ciemat.es/EPS2017PAP/pdf/P1.151.pdf)
[89] Blanken T. *et al* 2018 *Fusion Eng. Des.* **126** 87
[90] Lang P. *et al* 2018 *Nucl. Fusion* **58** 036001
[91] Felici F. *et al* 2019 Model-based design, simulation and testing of an electron temperature profile controller on ASDEX-Upgrade *Nucl. Fusion.* submitted
[92] Weiland M. *et al* 2018 *Nucl. Fusion* **58** 082032
[93] Maraschek M. *et al* 2018 *Plasma Phys. Control. Fusion* **60** 014047
[94] Valovic M. *et al* 2018 *45th European Physical Society Conf. on Plasma Physics (Prague, Czech Republic, 2–7 July 2018)* p P2.1075 (http://ocs.ciemat.es/EPS2017PAP/html)
[95] Aguiam D.E. *et al* 2016 *Rev. Sci. Instrum.* **87** 11E722

[96] Bobkov V. *et al* 2017 *Plasma Phys. Control. Fusion* **59** 014022
[97] Zhang W. *et al* 2017 *Nucl. Fusion* **57** 116048
[98] Kazakov Y.O. *et al* 2017 *Nat. Phys.* **13** 973
[99] Kazakov Y. *et al* 2018 Recent advances in ICRF heating of mixture plasmas: survey of JET and AUG experiments and extrapolation to JET-DT and ITER *Preprint: 2018 IAEA Fusion Energy Conf. (Gandhinagar, India, 22–27 October 2018)* [EX/8-1]
[100] Kappatou A. *et al* 2018 *45th European Physical Society Conf. on Plasma Physics (Prague, Czech Republic, 2–7 July 2018)* pO2.105 (http://ocs.ciemat.es/EPS2018PAP/pdf/O2.105.pdf)
[101] Schneider M. *et al* 2017 *EPJ Web Conf.* **157** 03046
[102] Lauber P. *et al* 2018 Strongly non-linear energetic particle dynamics in ASDEX Upgrade scenarios with core impurity accumulation *Preprint: 2018 IAEA Fusion Energy Conf. (Gandhinagar, India, 22–27 October 2018)* [EX/1-1]
[103] Salewski M. *et al* 2016 *Nucl. Fusion* **56** 106024
[104] Salewski M. *et al* 2018 *Nucl. Fusion* **58** 036017
[105] Garcia-Munoz M. *et al* 2019 *Plasma Phys. Control. Fusion* **61** 054007
[106] Sharapov S.E. *et al* 2018 *Plasma Phys. Control. Fusion* **60** 014026
[107] Zeeland M.A.V. *et al* 2008 *Plasma Phys. Control. Fusion* **50** 035009
[108] De Vries P. *et al* 2011 *Nucl. Fusion* **51** 053018
[109] Pau A. *et al* 2017 *Fusion Eng. Des.* **125** 139
[110] Pautasso G. *et al* 2017 *Plasma Phys. Control. Fusion* **59** 014046
[111] Fable E. *et al* 2016 *Nucl. Fusion* **56** 026012
[112] Hesslow L. *et al* 2017 *Phys. Rev. Lett.* **118** 255001
[113] Gobbin M. *et al* 2018 *Plasma Phys. Control. Fusion* **60** 014036
[114] Papp G. *et al* 2013 *Nucl. Fusion* **53** 123017
[115] Bandaru V. *et al* 2019 *Phys. Rev.* E **99** 063317
[116] Creely A.J. *et al* 2018 *Rev. Sci. Instrum.* **89** 053503
[117] Freethy S.J. *et al* 2018 *Phys. Plasmas* **25** 055903
[118] Pinzon J. 2018 Modelling and application of Doppler reflectometry for advanced turbulence studies on the ASDEX Upgrade tokamak and the TJ-II stellarator *PhD Thesis* Technical University Munich (TUM)
[119] Pinzon J.R. *et al* 2019 *Nucl. Fusion* **59** 074002
[120] Erofeev I. *et al* 2017 *Nucl. Fusion* **57** 126067
[121] Lebschy A. *et al* 2018 *Nucl. Fusion* **58** 026013
[122] Hornsby W. *et al* 2017 *Nucl. Fusion* **57** 046008
[123] Hornsby W. *et al* 2018 *Nucl. Fusion* **58** 056008
[124] Angioni C. *et al* 2017 *Nucl. Fusion* **57** 116053
[125] Schneider P. *et al* 2017 *Nucl. Fusion* **57** 066003
[126] Manas P. *et al* 2019 *Nucl. Fusion* **59** 014002
[127] Kappatou A. *et al* 2018 Energy confinement and performance of pure helium plasmas and helium seeded deuterium plasmas *Preprint: 2018 IAEA Fusion Energy Conf. (Gandhinagar, India, 22–27 October 2018)* [EX/P8-1]
[128] Luce T. *et al* 2018 *Nucl. Fusion* **58** 026023
[129] Fable E. *et al* 2019 *Nucl. Fusion* **59** 076042
[130] Bruhn C. *et al* 2018 *Plasma Phys. Control. Fusion* **60** 085011
[131] Angioni C. *et al* 2017 *Nucl. Fusion* **57** 022009
[132] Kappatou A. *et al* 2019 *Nucl. Fusion* **59** 056014
[133] Herrmann A. *et al* 2017 *Fusion Eng. Des.* **123** 508
[134] Herrman A. *et al* 2019 *Fusion Eng. Des.* accepted (https://doi.org/10.1016/j.fusengdes.2019.01.114)
[135] Pan O. *et al* 2018 *Plasma Phys. Control. Fusion* **60** 085005
[136] Labit B. *et al* 2019 *Nucl. Fusion* **59** 086020